Ultrasonic monitoring of friction contacts during shear vibration cycles

Alfredo Fantetti, Stefano Mariani, Luca Pesaresi, David Nowell, Frederic Cegla, Christoph Schwingshackl

Mechanical Systems and Signal Processing 161 (2021) 107966

Contents lists available at ScienceDirect

Mechanical Systems and Signal Processing

journal homepage: www.elsevier.com/locate/ymssp

Ultrasonic monitoring of friction contacts during shear vibration cycles

Alfredo Fantetti [a,*], Stefano Mariani [a], Luca Pesaresi [a], David Nowell [a], Frederic Cegla [a], Christoph Schwingshackl [a]

[a] Department of Mechanical Engineering, Imperial College London, Exhibition Rd, SW7 2BU London, UK

ARTICLE INFO

Article history:
Received 7 December 2020
Received in revised form 6 April 2021
Accepted 10 April 2021
Available online xxxx
Communicated by Xingjian Jing

Keywords:
Stick/slip identification
Ultrasound technique
Dynamic friction joints
Contact interface monitoring
Hysteresis loops
Tangential contact stiffness

ABSTRACT

Complex high-value jointed structures such as aero-engines are carefully designed and optimized to prevent failure and maximise their life. In the design process, physically-based numerical models are employed to predict the nonlinear dynamic response of the structure. However, the reliability of these models is limited due to the lack of accurate validation data from metallic contact interfaces subjected to high-frequency vibration cycles. In this study, ultrasonic shear waves are used to characterise metallic contact interfaces during vibration cycles, hence providing new validation data for an understanding of the state of the friction contact. Supported by numerical simulations of wave propagation within the material, a novel experimental method is developed to simultaneously acquire ultrasonic measurements and friction hysteresis loops within the same test on a high-frequency friction rig. Large variability in the ultrasound reflection/transmission is observed within each hysteresis loop and is associated with stick/slip transitions. The measurement results reveal that the ultrasound technique can be used to detect stick and slip states in contact interfaces subjected to high-frequency shear vibration. This is the first observation of this type and paves the way towards real-time monitoring of vibrating contact interfaces in jointed structures, leading to a new physical understanding of the contact states and new validation data needed for improved nonlinear dynamic analyses.

1. Introduction

Jointed structures use a wide range of friction joints to facilitate their assembly. Beyond their primary functions of joining two components, providing structural strength, and potentially sealing, friction joints are often the main source of damping in the assembly, and as such they have a large influence on the nonlinear dynamic response [1–3]. If the friction joints are not accurately modelled, they may lead to a poor design of the components used in structures such as aero-engines and turbomachinery, which can generate unwanted vibrations and wear at the interfaces [4,5] with consequent increased maintenance requirements and potential high cycle fatigue failures. To avoid such events, extensive work has been carried out in the past decades to improve modelling tools that describe the behaviour of such friction joints [6–9]. Many of these models base their predictive capabilities on the accurate discretisation of the contact interfaces to capture the underlying friction mechanisms across the interface and predict their impact on the nonlinear dynamic response [10–13]. Although these tools

* Corresponding author.
E-mail address: a.fantetti@imperial.ac.uk (A. Fantetti).

https://doi.org/10.1016/j.ymssp.2021.107966
0888-3270/

have been validated against global response data, leading to a high level of confidence in their overall capabilities, the correct modelling of the interface mechanisms remains a large unknown due to a lack of high-quality validation data from the contact interfaces. It is in fact challenging to capture what is happening during vibration cycles locally in the interface without interfering with the contact interface itself.

A few attempts have been made in the past to monitor sliding contact interfaces and provide insights into the underlying mechanisms. Non-contact techniques based on direct optical measurements have been used to study the contact of transparent materials [14–19], successfully observing changes in the real area of contact at the onset of slip. However, the requirement of at least one transparent medium to allow the optical access makes these approaches non-applicable for common metal to metal dry friction joints. To overcome some of the restrictions of impermeable materials, other optical measurement techniques have been proposed, such as Laser Doppler vibrometer measurements [20–23] or digital image correlation (DIC) with high-speed cameras [24–30], both of which have been used to monitor the motion of the boundaries of friction joint interfaces during a vibration cycle. These studies measured friction hysteresis loops, which are the typical load–deflection curves representing the sliding behaviour of contact interfaces under vibration, making it possible to observe several contact phenomena, such as stick–slip transition at the edges of the contact, opening and closing of the contact and identification of permanent gaps. The main limitation of both laser and DIC techniques is that measurement points are not located exactly at the interface but tens of micrometers away from it, specifically on the side of the contacting components. Therefore, they only provide one- or two-dimensional information from the edge of the contact interface, without providing any insight into the behaviour of the central part of the contact. The information on the full contact behaviour is then still relying on numerical models to predict what is happening inside, with only few validation data coming from experimental evidence at the edges.

An alternative method to access non-transparent contact interfaces is the use of active ultrasound and/or acoustic emissions (i.e. passive ultrasound). Previous studies have used acoustic emissions [31–34] measured in the near field around the contact to detect the onset of slipping. The main challenges for dynamic applications would be to isolate the frictional noise from other sources of noise in the test (structural vibration, shaker etc.) and to localise the slipping area. In contrast to this, active ultrasound has been mainly used to study tribological contacts under static or quasi-static conditions [35], providing e.g. detailed information on the contact stiffness [36–44]. Unfortunately, this information alone is not adequate to monitor the different friction mechanisms during a high-frequency vibration cycle (e.g. stick–slip transitions, separation, or normal load variations). In fact, while the underlying physics are reasonably well known in full stuck contacts, it is still rather unclear what happens when the contact starts to slide at high frequency since only a few studies attempted to use active ultrasound to investigate sliding contacts [45–47].

Building on the authors previous work [46], this paper describes the novel use of an ultrasonic technique to experimentally investigate such interfaces during sliding in combination with numerical simulations to support the interpretation of the results. The aim is to provide novel insights into the underlying physical phenomena that drive the friction mechanisms (e.g. normal load distribution, stick–slip transitions and microslip distribution). A direct comparison is assessed between the contact stiffnesses obtained from ultrasound measurements and from the more traditional hysteresis loop measurements. The ultrasound variability within single vibration cycles is measured at different time instants, revealing for the first time a modulation of the ultrasound signal during stick and slip transitions of the frictional contacts. The findings provide novel insights into the physics of the contact and form the basis for future real-time interface monitoring of vibrating jointed structures, needed to prevent failures and provide validation data for state-of-the-art numerical models.

2. Background on ultrasonic techniques for contact measurements

Ultrasonic techniques use acoustic waves at frequencies above the human audible range (20 kHz). They are traditionally used for crack detection, material property characterisation and imaging, but have also been used to study contact interface properties [35,39,45]. In this latter application, a transducer, usually piezoelectric, generates ultrasonic waves (longitudinal or shear) that travel through the host medium by pushing and pulling atoms, until reaching the contact interface. At the contact interface, some of the wave energy is transferred to the mating surface and some is reflected depending on, among other things, the degree of contact between the two contacting surfaces. When two rough surfaces are pressed against each other, contact occurs at the asperity peaks. Ultrasound passes through the contacting regions but is almost entirely reflected at the air-filled gaps. This reflection is due to the large acoustic impedance mismatch between structural materials and air. The amount of transmission/reflection can be therefore used to study the contact properties of the interface. For example, changes in reflection and transmission are linked to variations in the contact stiffness of the interface, since such stiffness appears in the stress/strain equilibrium boundary conditions that govern the sound wave propagation at the interface [48,45]. Tattersall [48] derived the relationships for the reflection, while Kendall and Tabor [45] derived them for the transmission. When the materials across the interface are identical, their derived relationships are the following for reflection and transmission respectively:

$$R = \frac{1}{\sqrt{1 + 4K_{US}^2/(2\pi f Z)^2}} \tag{1}$$

$$T = \frac{2}{\sqrt{4 + (2\pi f Z)^2 / K_{US}^2}} \tag{2}$$

where K_{US} is the ultrasonically estimated contact stiffness per unit area expressed in N/mm^3 (either normal or tangential depending on whether longitudinal or shear ultrasonic waves are used respectively), f is the frequency of the ultrasonic wave [Hz], and $Z = \rho c$ is the acoustic impedance of the material, where ρ is the density [kg/m^3] and c is the velocity of the ultrasonic wave [m/s] in the material. R and T are respectively the reflection and transmission coefficients. These coefficients vary between 0 and 1 and indicate the degree of ultrasonic reflection/transmission at the contact. They are obtained by dividing the measured reflection/transmission by the possible maximum reflection/transmission for the investigated experimental setup, as better explained in Appendix A for the reflection coefficient. By experimentally measuring those coefficients, it is possible to quantify the contact stiffness, K_{US}. Note that the two K_{US} in Eqs. (1) and (2) are expected to be equivalent, although it was not possible to test this equivalence in this study, where only Eq. (1) (i.e. K_{US} linked to the reflection coefficient) has been used. This is better explained in Section 4.3.

Eqs. (1) and (2) hold well when the wavelength of the ultrasonic wave (i.e. the inverse of its frequency multiplied by the ultrasonic wave velocity) is much larger than the width of the gaps at the contact interface. In fact, when the wavelength is comparable in size with the air gaps, the waves undergo complicated scattering patterns governed by the exact shapes of the gaps. Instead, at larger wavelengths, the proportions of transmitted/reflected ultrasonic waves are almost solely dictated by the stiffness of the interface. A more detailed description of the behaviour of ultrasonic waves at different frequencies and wavelengths can be found in [39]. While the reflection/transmission is frequency dependent for the above mentioned reasons, the contact stiffness is frequency independent, being solely a property of the contact interface [38,45,39].

Most of the ultrasonic studies improved the physical understanding of static contacts [35], providing e.g. detailed information on the contact stiffness [36–44], but only few have attempted to use ultrasound to investigate sliding or dynamic contacts [38,45–47,49,50], with the pioneering work of Kendall and Tabor [45] being one of the first. They acquired ultrasonic waves in a pin-on-disc setup, finding that the ultrasound transmission increases with sliding because of the junction growth phenomenon, which is described in Section 5.1. A further step in the ultrasonic investigation of sliding contacts has been achieved with studies [38,46] that performed a direct comparison between ultrasound measurements and hysteresis loops, which are the load–deflection data of two vibrating contact interfaces as shown in Fig. 1. Mulvihill et al. [38] used ultrasound to monitor quasi-static contacts undergoing sliding while simultaneously measuring hysteresis loops with the DIC technique. They confirmed the hypothesis made by Kim et al. [37] that the ultrasound technique measures an elastic stiffness due to loading and unloading cycles on the asperities induced by the travelling ultrasonic wave. These studies showed that the ultrasonically measured stiffness was consistently larger than that obtained from hysteresis loops with DIC or laser measurements [38,46], most probably because the latter also includes the bulk deformation in addition to the asperity contribution [51]. This difference is investigated in Section 4.3, where experimental measurements are compared to numerical simulations of the bulk deformation. Although Mulvihill et al. [38] studied sliding contacts, their measurements were performed under quasi-static conditions. Instead, Pesaresi et al. [46] performed ultrasonic measurements during high-frequency vibrations, and observed that the ultrasound technique is sensitive to the evolution of contact interfaces during sliding. In their preliminary work, only few datapoints were acquired within a single vibration cycle, thus making it difficult to assess to which extent it is possible to detect changes in contact states within a vibration cycle. Building on their work, in the present study more datapoints are acquired within single vibration cycles, providing unprecedented insights into the friction mechanisms of sliding interfaces.

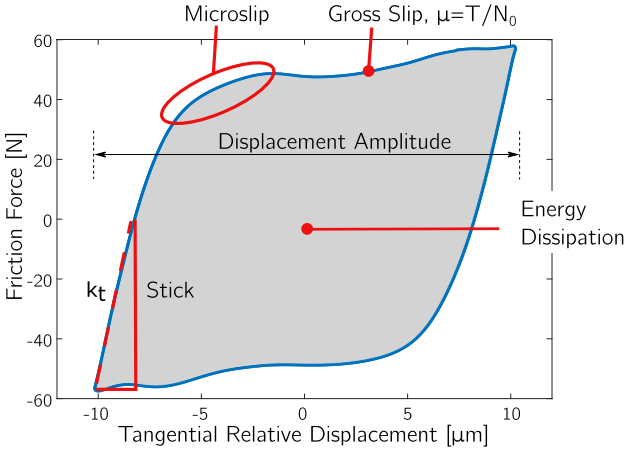

Fig. 1. Friction hysteresis loop, the load–deflection curve resulting from the vibrating motion of two contact interfaces. μ is the friction coefficient, T is the friction force during gross slip, N_0 is the normal load and k_t is the tangential contact stiffness.

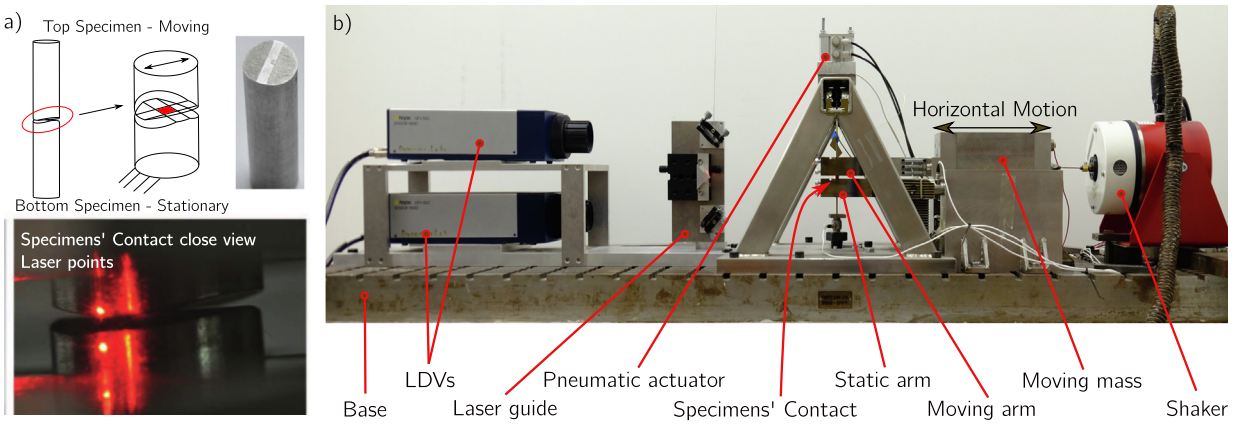

Fig. 2. (a) Specimen arrangement for the flat-on-flat contact; (b) Photo of the friction rig [52].

3. Experimental setup

This section shortly describes the high-frequency friction rig [52] that is commonly used to provide input contact parameters for turbomachinery applications by measuring friction hysteresis loops. A typical hysteresis loop measured from the rig is shown in Fig. 1. The hysteresis loop is the load–deflection curve resulting from the vibrating motion of two contact interfaces, and is characterised by three friction regimes, (i) stick, (ii) microslip and (iii) gross slip. The stick regime occurs during the initial phase of relative motion, in which asperities are still stuck together. As the load increases, some asperities remain stuck, while others enter relative sliding, thus leading to the microslip regime. When the friction force reaches the friction limit, the whole interface enters the gross slip regime. From the loops, tangential contact stiffness, k_t, and friction coefficient, μ, can be extracted as shown in Fig. 1. These contact parameters are the required input to nonlinear dynamic simulations of jointed structures and must be correctly measured as they strongly affect the vibrational behaviour of the whole structure [4,5,53].

3.1. Description of the friction rig

The friction rig generates an oscillating sliding motion between a pair of cylindrical specimens with a square flat-on-flat area of contact as shown in Fig. 2a. Fig. 2b shows the rig, which is composed of a moving block (moving mass and moving arm) that oscillates horizontally under the harmonic excitation of an electrodynamic shaker. The top specimen is clamped to the moving arm, whilst the bottom specimen is clamped to the static arm. The relative displacement between the specimens is measured using two Laser Doppler vibrometers pointed very close to the contact interface, as shown in Fig. 2a, to ensure that the measured displacement comes from the contact interface itself, and the bulk deformation contribution is minimised. The friction force transmitted in the contact is measured via three dynamic load cells that ground the static arm to the base of the rig. During the test, a continuous contact is ensured via a pneumatic actuator that applies a normal load on the top specimen. A more detailed description of the rig is given in [52]. Typically, the rig is operated with a 100 Hz harmonic excitation and displacement amplitudes in the range of 0.1–30 μm, which cover all stick, microslip and gross slip regimes.

3.2. Experimental setup with ultrasound

The friction rig has been upgraded by Pesaresi et al. [46] to record ultrasonic waves simultaneously with hysteresis loops. In this study, improvements in the experimental procedure were implemented that enabled a novel real-time investigation of the ultrasound variability within a single hysteresis loop.

304 stainless steel specimens have been designed to accommodate a shear transducer (NOLIAC CSAP02) that generates and receives shear waves. Shear waves were preferred over longitudinal waves to enable a more accurate comparison with hysteresis loop measurements. The specimen is shown in Fig. 3 and consists of a 28 mm long cylindrical holder, with a 10 mm diameter, coupled with a threaded head on which the shear transducer is glued by using a two-parts Loctite Double Bubble epoxy resin capable of a shear strength of 9 MPa. A more detailed description is given in [46]. The specimen interface is nominally flat and is obtained by carefully hand polishing with two different grades of sand paper: first, 800 grit for coarse and bulk material removal and then, 2500 grit for smooth and finer surface finish, leading to a final roughness value Ra of about 0.5 μm. The contact interface is 3 mm wide and approximately 10 mm long, and the two mating specimens are rotated by 90° with respect to each other, hence obtaining a 3 by 3 mm square nominal area of contact as shown in Fig. 3c. The ultrasonic transducer has an area of 25 mm^2 that is larger than the area of the contact interface (9 mm^2), thus ensuring that the whole contact area is insonified with ultrasonic energy. The effects of this area mismatch need to be taken into account for

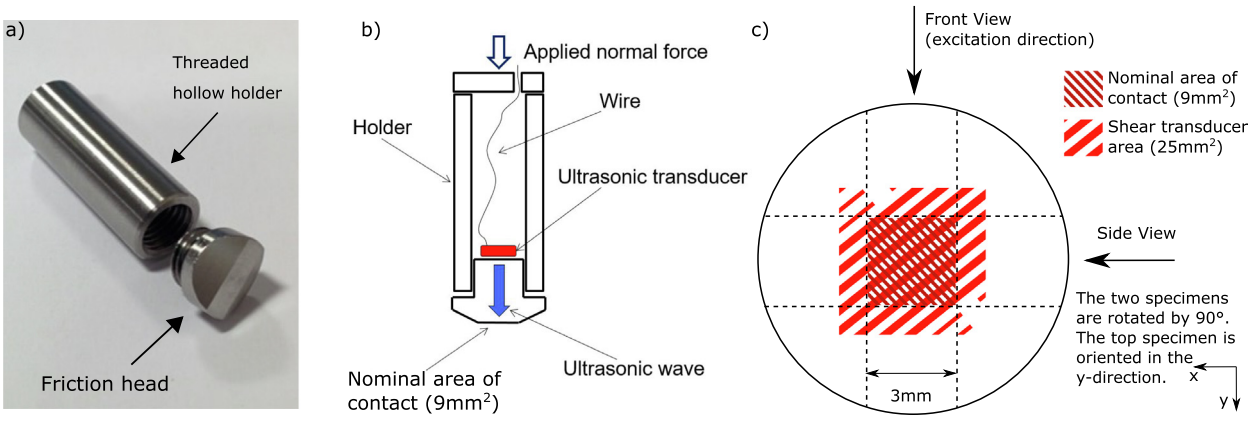

Fig. 3. Specimen designed to accommodate an ultrasonic transducer: (a) Photo; (b) Scheme; (c) Specimens top view. Shear waves are polarized in the y-direction.

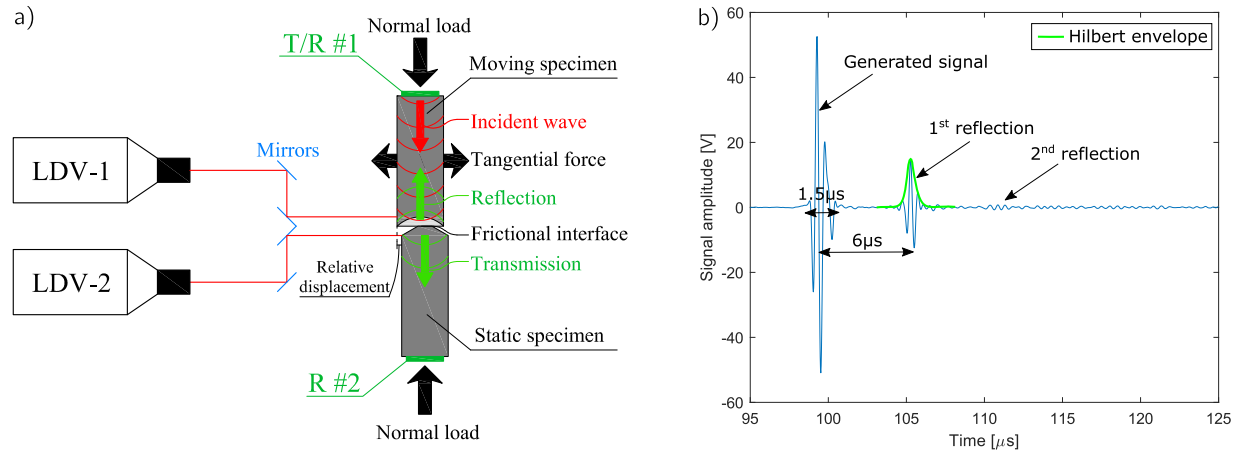

Fig. 4. (a) Simplified scheme of the ultrasonic experimental setup (note that the exact position of the ultrasonic transducers T/R#1 and R#2 is that shown in Fig. 3(b); (b) Incident signal characteristics.

the correct estimation of the reflection coefficient R at the interface, which is required as input in Eq. 1 to obtain the tangential contact stiffness; this was done via numerical simulations, as described in Appendix A.

The experimental setup is schematically shown in Fig. 4a. Ultrasonic shear waves are sent to the contact interface by exciting a transmitting/receiving piezoelectric patch labelled T/R#1, which is installed on the moving specimen and which operates in pulse-echo mode. This transducer is paired with the second receiving patch labelled R#2, which is installed on the static specimen and only acts as a receiver, hence working in pitch-catch mode. This setup allows for the simultaneous measurement of both reflection and transmission of the ultrasound signal amplitude from the frictional interface. The transducer T/R#1 needs an input voltage signal to generate shear waves. The voltage signal is generated by the arbitrary function generator of a handyscope HS5 (TiePie Engineering), which is amplified by an in–house linear 10x drive amplifier. The transducer generates a shear wave that travels from the top of the moving specimen down to the contact interface. When the wave reaches the interface, a portion of its energy is reflected to the T/R#1 transducer, and a portion is transmitted to the R#2 transducer.

A typical signal recorded by the first transducer is shown in Fig. 4b. The handyscope generates a 3-cycle Hann windowed burst at 2 MHz (the resonance frequency of the loaded transducer). After being generated and amplified, the burst is sent to the T/R#1 transducer. The first reflection from the contact interface arrives after 6 µs, and the second, much weaker, reflection is also seen after further 6 µs. This travel time depends on the length of the path between transducer and contact interface, and on the shear wave velocity, which was determined to be 3060 m/s for the particular steel used by dividing the path length by the travel time. The receiver transducer R#2 receives the first and second transmission at the same time instants at which the reflections are received by T/R#1, since the travelling distance is the same for both specimens. In this investigation, multiple bursts are sent within a single hysteresis loop at a frequency of 10 kHz, while Pesaresi et al. [46] only sent one

burst per loop. Consequently, the ultrasound variability within a single hysteresis loop can be observed, thus making it possible to assess whether the ultrasound behaviour depends on the changing friction regimes (stick, microslip and gross slip). In addition, ultrasound transmission and hysteresis loops are synchronised to localise where each burst lies within the hysteresis loop. A 6th order digital Butterworth band-pass filter with cut-off frequencies of 1.5 and 2.5 MHz is applied to the ultrasonic signal to remove noise outside the signal bandwidth. Next, a Hilbert transform is applied to the signals to identify the exact peaks of the first reflection and transmission signal (as shown in Fig. 4b). These peaks are then used in the data analysis of the tests described in the following sections.

4. Vibration tests under stuck conditions and different normal loads

The goal of this measurement campaign is to assess the feasibility of the ultrasound technique to measure the tangential contact stiffness by means of a direct comparison with hysteresis measurements. Vibration tests were conducted under a harmonic excitation of 100 Hz on the specimens described in Section 3.2 and hysteresis loops were recorded simultaneously with the ultrasound signals. The loops were recorded at a fixed displacement amplitude of 0.4 μm, which is small enough to obtain a stuck[1] regime without gross slip and at different normal loads. Tests were conducted with the specimens initially not in contact (i.e. 0 N normal load), then increasing the normal load in multiple steps up to 400 N, and finally decreasing it in the same number of steps back to 50 N to check for repeatability (see the loading sequence in Table 1). For each normal load, 10 consecutive hysteresis loops were recorded and, at the same time, 100 ultrasound bursts equidistant in time were sent during each loop to investigate the ultrasound variability within the loop. Note that hysteresis loops were not recorded at the 0 N normal load case, since the specimens were not in contact; this scenario is clearly associated to a null tangential contact stiffness.

4.1. Hysteresis loop measurements

The measured hysteresis loops from the friction rig are shown in Fig. 5a. All the loops are in the stuck regime with no slip occurring because of the low displacement amplitude. As the normal load increases, the gradient of the hysteresis loops increases as well, indicating that the tangential contact stiffness, k_t, increases with the normal load. In fact, k_t is determined by fitting a line to the collapsed loop. Fig. 5b shows the resulting mean k_t values as a function of the normal load, where each error bar indicates two times the standard deviation (i.e. 95% of the values) of the 10 consecutive hysteresis loops measured at each normal load. As mentioned already, the tangential contact stiffness increases with the normal load, approaching an asymptotic limit towards the higher loads, a behaviour that was also observed in previous studies [25,54–57]. This increase in the contact stiffness is linked to the increase in the number and size of the individual contact regions, resulting in a larger real area of contact and in more interactions of asperities at the interface [45,58]. Here, the stiffness increases roughly tenfold with the increasing normal load, from low values of 10 N/μm for a 7 N normal load to about 100 N/μm for a 400 N normal load. The relative standard deviation is in the range of 10–50%. Notably, loading and unloading steps in Fig. 5b follow roughly the same curve, highlighting the good repeatability of the measured contact stiffness.

4.2. Ultrasonic measurements

Ultrasound bursts were sent every 100 μs, leading to 100 pulses per loop. The measurement was repeated for each of the 10 consecutive loops, leading to 1000 consecutive recorded bursts for each test condition (i.e. at each normal load). The ultrasound measurements were synchronised with the hysteresis loop measurements of Fig. 5a by measuring them on the same handyscope device that contains several time synchronised input channels. In this way, the position of the bursts within each loop could be identified.

Initially, a static test was conducted by only varying the normal load (with specimens not in motion), then followed by the dynamic tests described in the previous section, in order to check if any difference in reflection/transmission appeared when specimens were still or in stuck vibration at 0.4 μm. Peaks in reflection and transmissions were computed following the procedure described in Section 3.2, leading to the results shown in Fig. 6 for the different normal loads. The ultrasound measurements from static and stick tests give nearly identical response in terms of mean values and noise. Three observations can be made:

(i) the stuck transmission values of Fig. 6b remain constant throughout all 10 vibration cycles, and are very similar to the static measurements of Fig. 6a, suggesting that low displacement amplitudes do not noticeably affect the ultrasound transmission. This is probably because the asperities in contact do not slide, and consequently the real contact area, which affects the transmission, remains unchanged during a vibration cycle. It can be concluded at this stage that the ultrasound technique cannot be used to detect if a contact is fully static or is undergoing elastic deformations in the stick regime. The same conclusions apply to the reflection, which is not shown for the sake of conciseness;

[1] Note that a full stuck regime is never achievable in practise, since a small part of the contact interface will always exhibit microslip. However, at very low displacement amplitudes, the portion of interface in microslip is assumed to be negligible compared to the major remaining portion of interface in stuck condition.

Table 1
Summary of test loading conditions for the vibration tests under stuck conditions.

Test conditions	Static normal load [N]	Displacement amplitude [μm]
Room temperature 9 mm^2 flat nominal area of contact 100 Hz harmonic excitation 304 Stainless steel specimens	0, 7, 20, 50, 100, 150, 200, 250, 300, 350, 400 350, 300, 250, 200, 150 100, 50	0.4

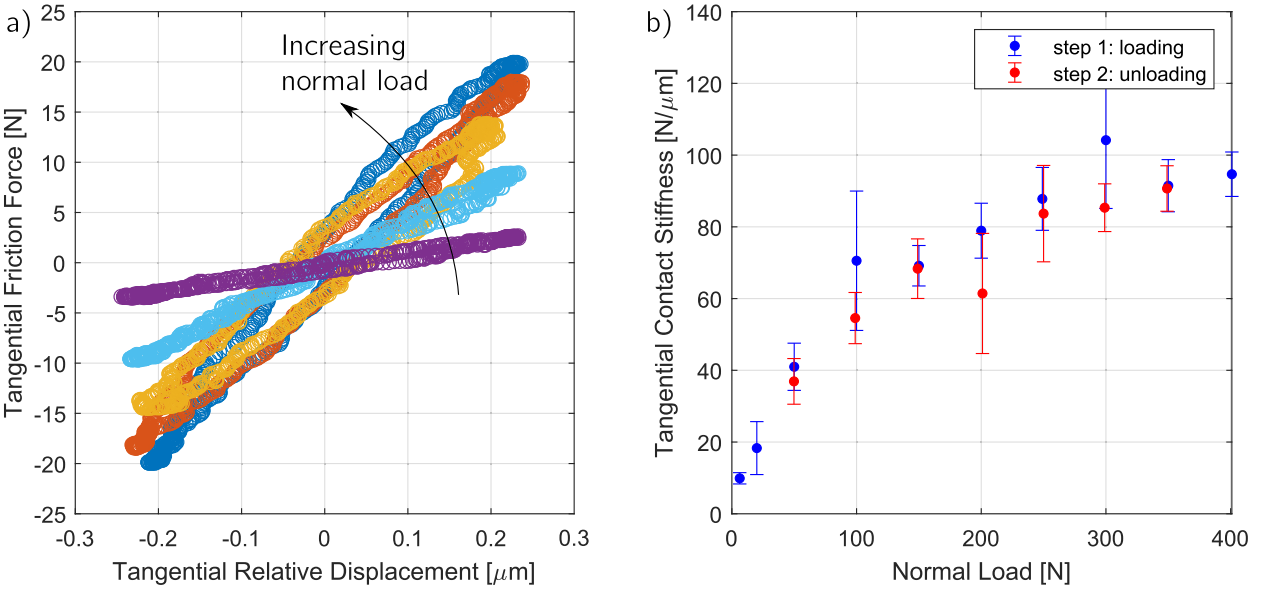

Fig. 5. Vibration tests under stuck conditions: (a) Hysteresis loops measured in stuck condition at different normal loads; (b) Tangential contact stiffness extracted from hysteresis loops, k_t, as a function of the normal load.

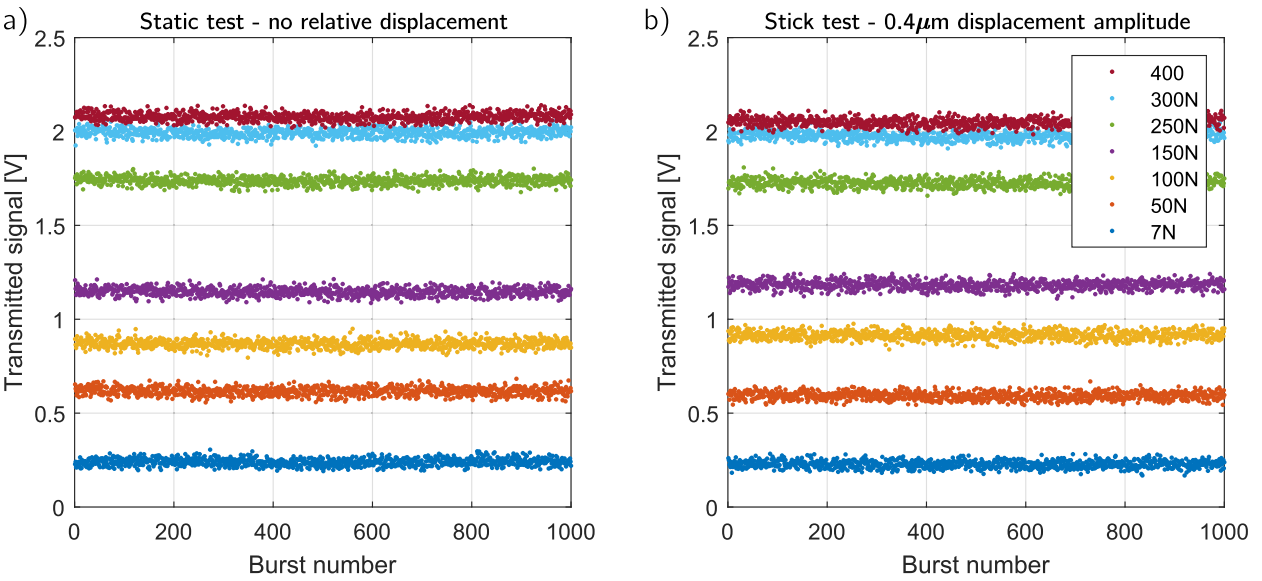

Fig. 6. 1000 peaks in the transmitted signals: (a) Static test; (b) Stick test at 0.4 μm displacement amplitude for some normal loads from the measurements of Fig. 5.

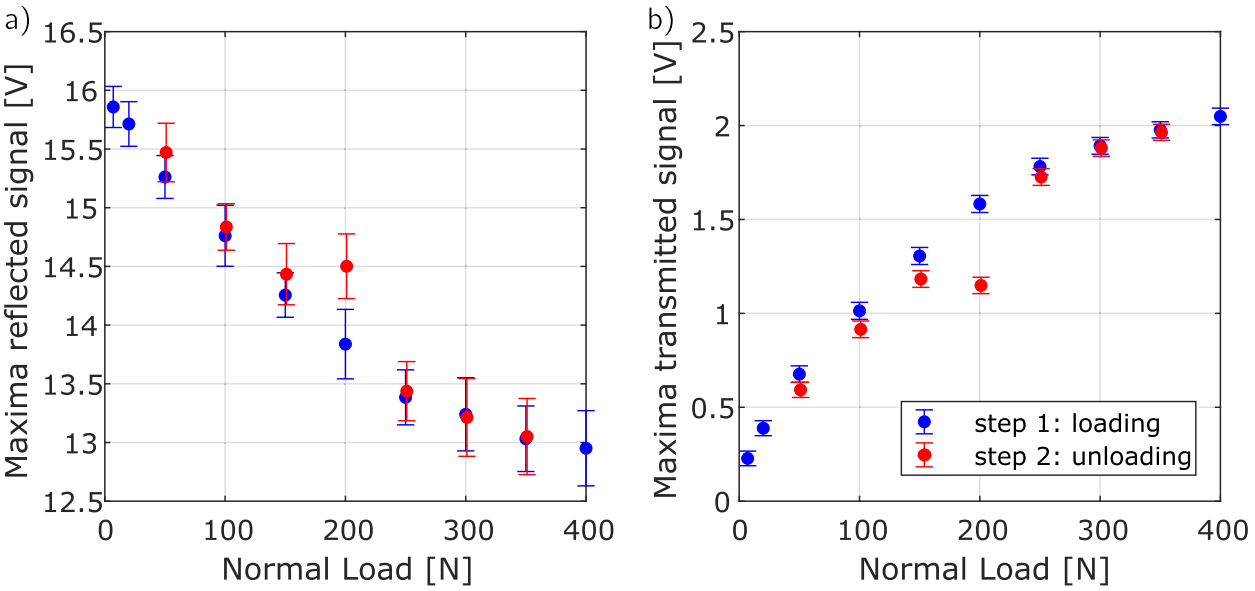

Fig. 7. Vibration tests under stuck conditions: (a) Reflected and (b) Transmitted signals as a function of the normal load.

(ii) It can also be observed that the ultrasound transmission increases with the normal load while the reflection decreases, confirming previously reported trends [36,37,39,42,43,45,59]. This is better illustrated in Fig. 7, where the mean of the peaks of the reflected and transmitted signals are plotted as a function of the normal load. Each error bar represents two times the standard deviation (i.e. 95% of the values) of the 1000 bursts that cover the 10 consecutive hysteresis loops recorded at each normal load. The transmitted signal follows a similar trend to that of the contact stiffness in Fig. 5b, since the increasing number and size of the individual contact regions with the normal load lead to a higher ultrasound transmission along with an increase in the tangential contact stiffness. For the same reason, a weaker signal is reflected as the normal load increases. The relative standard deviation is in the range of 3–20%, which is more than three times lower than that observed during the hysteresis measurements, indicating that ultrasound measurements exhibit less noise than the hysteresis data when stick vibration tests are performed. The hysteresis measurement poorer performance is probably caused by the fact that two different time signals are needed (force and displacement), while for the ultrasound only a single time signal is needed, with a consequent reduced noise;
(iii) it is interesting to note that in Fig. 7b the transmission at 200 N during the unloading is lower than expected (and conversely the reflection is larger). The same drop is also observed in the contact stiffness measured from the hysteresis loops as shown in Fig. 5b and might have occurred due to an unwanted drop in the normal load during the experiment. The drop has been captured by both measurement techniques, confirming the strong correlation between ultrasound, hysteresis measurements and normal load.

To quantitatively analyse the correlation between the contact stiffness extracted from the hysteresis loops, k_t, and the contact stiffness per unit area extracted from the ultrasonic measurements, K_{US}, Eq. 1 is used to obtain K_{US} from the experimental reflection coefficient. This coefficient is estimated with the methodology described in Appendix A and specifically via Eq. A.1. Fig. 8a plots the reflection coefficient evaluated in this manner, showing that it drops with increasing normal load, following the identical trend of the reflected signal in Fig. 7a. The reflection coefficient seems to approach an asymptotic limit of $R = 0.75$ at 400 N. In theory, the asymptote should be reached when a fully bonded contact is present, leading to an $R = 0$ reflection coefficient as a result of a null reflection and maximum transmission. Since specimens are still in a fully elastic regime due to the relatively low loads (e.g. 400 N over 9 mm^2 equals a nominal mean pressure of 50 MPa at the bulk), the material is far from reaching a full contact, which only occurs when loads are so large that the material plastically deforms, and asperities flatten completely and merge. Consequently, the asymptote observed in Fig. 8a must have a different explanation.

Similar large asymptotic values in the reflection coefficient have been observed in previous studies [39,60], and their origin has been attributed to the fact that the plastic flow occurred almost entirely within the first normal loading step [37,51,61], during which asperities flatten to a shape conformal with the opposing surface. In each subsequent loading and unloading step, the conformity was partially maintained even after the load removal, and the same points on each surface made contact again, thus leading asymptotically to the value previously reached with the largest load. In fact, during the first loading, measured trends were linear (i.e. no asymptote at the last loading step), but when subsequent unloading and reloading cycles were performed, an asymptote appeared [39,60]. The same hysteretic behaviour was reported in studies that used optical measurements to estimate real areas of contact under increasing normal loads [17,62], all confirming exist-

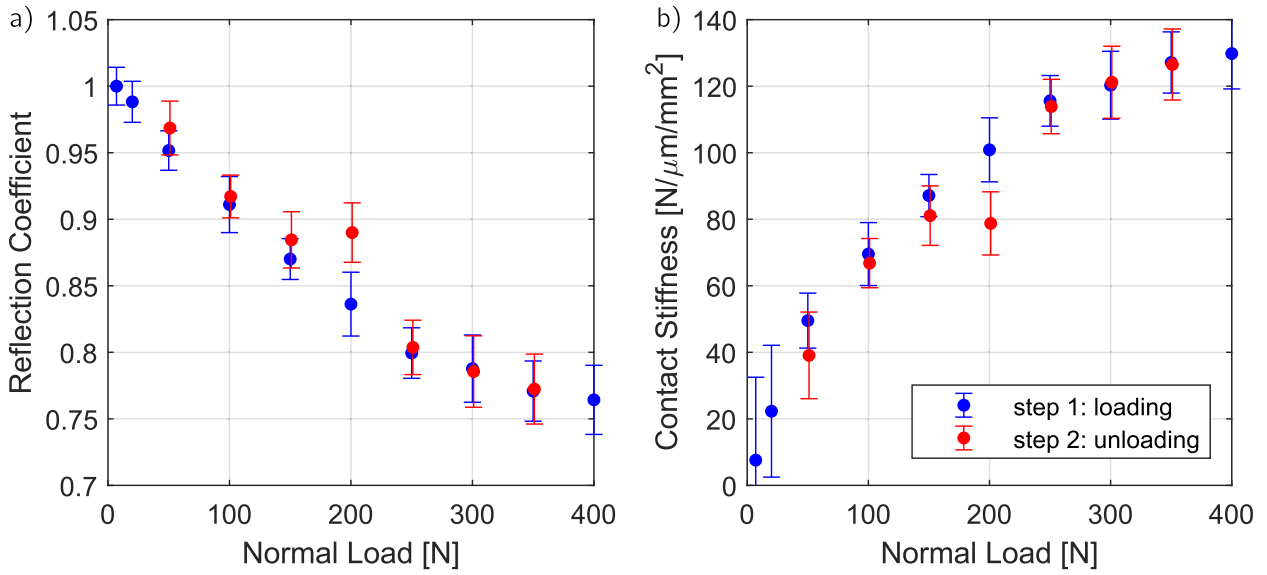

Fig. 8. Vibration tests under stuck conditions: (a) Reflection coefficients obtained from values of Fig. 7a; (b) K_{US}, tangential contact stiffness obtained from the reflection coefficient by using Eq. 1 (Tattersall formulation).

ing elastoplastic descriptions of contact mechanics [37,61,63]. In the case of the measurements of Fig. 8a, a series of pre-loading and unloading cycles of the normal load were performed to initialise the experimental setup, where the ultrasound transmission/reflection was not measured, and hence the results shown here were obtained for the already plastically deformed contact interface. It is worth mentioning that this plastic deformation is only induced by the applied static normal load, while the oscillating tangential load that generates hysteresis loops only leads to fully elastic displacements because of the very low displacement amplitudes. If the normal load were to be further increased, though this is not possible with the available test setup, new contact spots would appear and the asperities would further deform, thus increasing the contact stiffness and hence reducing the reflection coefficient until full contact is reached, eventually leading to a null reflection. This phenomenon is not commonly considered in nonlinear dynamics analyses of jointed structures subjected to vibration [1,6], although it can lead to large variations in the system behaviour especially during the first loading cycles.

4.3. Comparison between contact stiffnesses obtained from hysteresis loops and ultrasonic measurements

Once the reflection coefficients were obtained, K_{US} values were calculated from Eq. 1 for different normal loads, with the ultrasonic wave frequency, f = 2 MHz, the density, ρ = 8000 kg/m^3, and the velocity, c = 3060 m/s. Results are plotted in Fig. 8b, showing that K_{US} reaches a clear asymptote at around 400 N normal load, similarly to the contact stiffness, k_t, obtained from hysteresis measurements in Fig. 5b, highlighting the physical relationship between the two measured stiffnesses. It is worth noting that the K_{US} obtained from Eq. 1 is a stiffness per unit area expressed in N/μm/mm^2, while the k_t measured from hysteresis loops is expressed in N/μm. As described in Appendix A, the reflection coefficient needed for the K_{US} calculation is estimated by taking as a reference the 9 mm^2 nominal area of contact, and therefore the resulting K_{US} is normalised by that nominal area of contact. By multiplying the K_{US} values by 9 mm^2, a k_{us} in N/μm is obtained (note that the latter is indicated in small letters to differentiate it from the K_{US} values expressed in N/μm/mm^2). The comparison between the ultrasonic k_{us} in N/μm and the hysteretic k_t is given in Fig. 9a, showing that k_{us} values are more than 10 times larger than those obtained from the hysteresis loops. This mismatch in values has also been observed in the only two previous studies [38,46] in which a direct experimental comparison between the two techniques was assessed. The large discrepancy can be most likely attributed to the fact that the contact stiffness obtained from hysteresis loops includes, in addition to the asperity contribution captured by the ultrasounds [51], also the bulk deformation between the laser measurement points. The FE analysis shown in Appendix B helps in the validation of this hypothesis by estimating, at 361 N/μm, the stiffness solely due to the bulk deformation, k_{bulk}. Stiffnesses due to both bulk deformation and contact interfaces can be summed in series to estimate stiffness values that, at a first approximation, should be equivalent to those extracted from hysteresis loops according to:

$$k_{eq} = \left(\frac{1}{k_{bulk}} + \frac{1}{k_{us}}\right)^{-1} \tag{3}$$

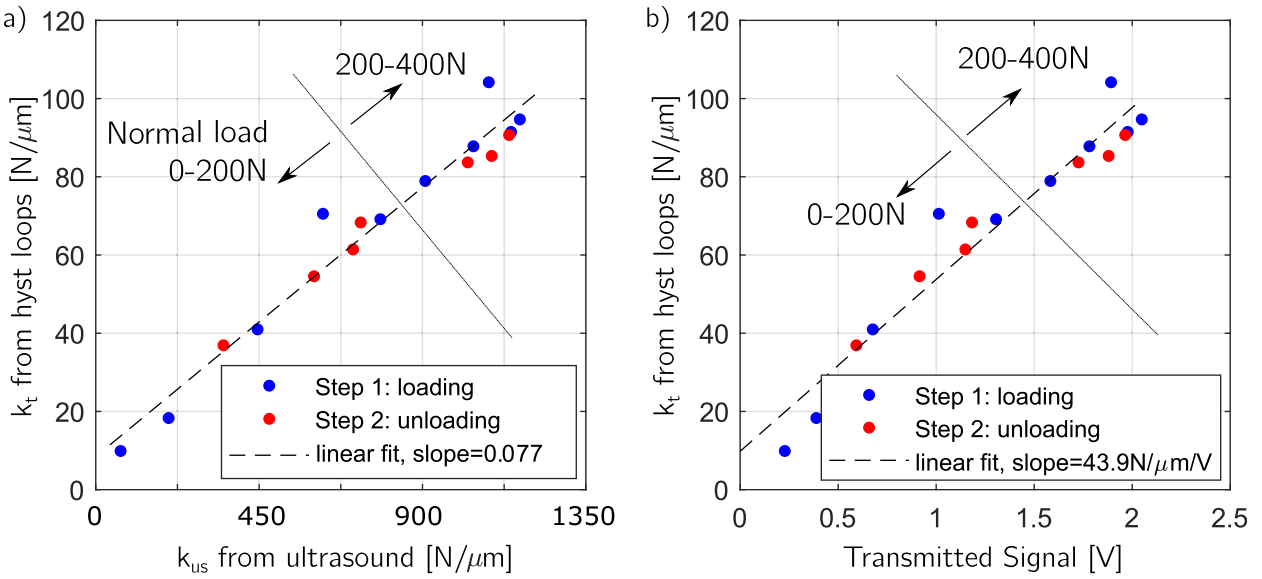

Fig. 9. Vibration tests under stuck conditions – each point corresponds to a different normal load: (a) k_t from hysteresis loops vs k_{us} from ultrasonic reflection; (b) k_t from hysteresis loops vs ultrasonic transmitted signal.

Where k_{us} is in N/μm (see x-axis of Fig. 9a), and is obtained by multiplying the K_{US} values of Fig. 8b by 9 mm^2, which is the nominal area of contact of the specimens. It is worth stressing that k_{eq} can only be considered as an approximate value, since this analytical formulation directly links static and dynamic phenomena occurring over a wide frequency range (static bulk stiffness, oscillations at 100 Hz and ultrasonic waves at several MHz).

The resulting k_{eq} from Eq. 3 is plotted in Fig. 10, where it is compared with the actual k_t measured from hysteresis loops (the same already shown in Fig. 5b). The mismatch between k_t and this equivalent stiffness is now significantly reduced compared to the larger mismatch with the k_{us}, thus partially confirming that the bulk deformation term plays a key role on this comparison. However, the discrepancy is still relatively large, indicating that the specimen bulk deformation is not the only compliance missing in the ultrasonic stiffness. A further possible source of compliance would be the rotation of the test rig arms due to the bending described in Appendix C. The effect of this bending on the rotation-induced displace-

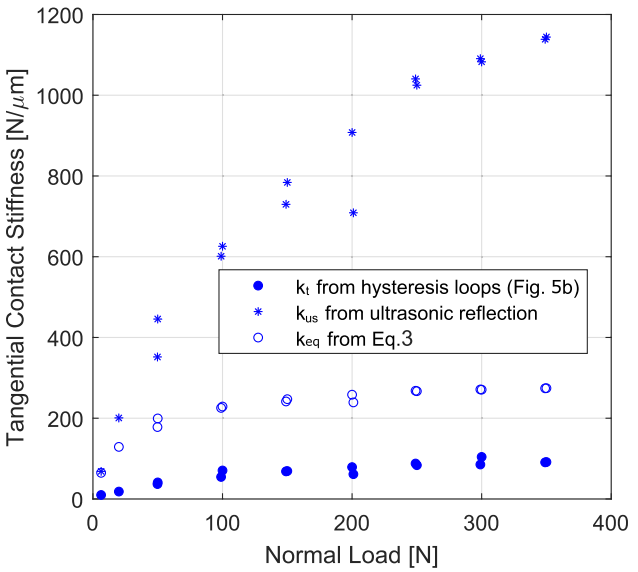

Fig. 10. Vibration tests under stuck conditions: comparison of tangential contact stiffness extracted from hysteresis loop, k_t; from ultrasonic reflection measurements, k_{us}; and from Eq. 3, k_{eq}, which includes the asperity interface contribution (i.e. k_{us}) and the bulk deformation contribution (i.e. stiffness k_{bulk} obtained from the FE model of Appendix B).

ment was therefore quantified, both numerically and experimentally, and found to be negligible (results not presented here for conciseness). Another reason for the stiffness mismatch can be that ultrasound might only be affected by the compliance due to the interface roughness, and not by the compliance coming from the interface waviness, which is at a slightly larger length-scale than that of the asperities (but at a smaller length-scale than that of the bulk, and therefore not captured by the FE model with ideal flat contacts). Part of this hypothesis has already been investigated in a previous work of the authors [4], where detailed scans of the contact interfaces were shown before and after analogous hysteretic tests. That study showed that the interface had a large effect on both hysteresis loops and contact parameters, especially at the beginning of the test until a steady state was reached due to the development of a full worn area of contact. In order to minimise this effect, all tests presented in this paper have been performed with the specimens already in a full worn steady-state condition.

Finally, it is worth noting that K_{US} could also be computed from the transmission coefficient, T, by using Eq. 2 as suggested by Kendall and Tabor [45]. However, the transmission coefficient cannot be readily computed via a formula analogous to Eq. A.1, as already done for the reflection coefficient. In fact, it is not possible to compute the ratio of the transmission amplitudes in "no contact" and "bonded contact" configurations, as defined in Appendix A, due to the absence of any transmitted signal in the "no contact" configuration, since the two specimens are fully detached and no signal is transmitted. Nevertheless, the transmitted signal can still provide information on the contact stiffness since it is linearly related to the transmission coefficient, which in turn is linearly related to the contact stiffness according to Eq. 2. This linear relationship is indeed confirmed by Fig. 9b, where the contact stiffness from the hysteresis loops is plotted against the ultrasonic transmitted signal for different normal loads. This is the first time, to the best of the authors knowledge, that such a direct comparison between hysteresis loops and transmission has been presented, further confirming the validity of the well-established Eq. 2.

4.4. Summary of vibration tests under stuck conditions

The results of the previous sections have demonstrated the existence of a strong correlation between hysteresis measurements and ultrasound reflection/transmission measurements. An increase in the contact stiffness, obtained with both techniques, was observed as the normal load increased. This is in good agreement with existing literature. A direct comparison between contact stiffness values obtained from hysteresis measurements and ultrasound measurements showed a linear relationship, although the ultrasonic stiffness was roughly 10 times larger than that obtained from hysteresis loops. This mismatch was largely attributed to the bulk deformation that is included in the hysteresis measurements and that instead is not captured by the ultrasonic measurements. This hypothesis was supported by FE simulations that estimated the bulk contributions. This bulk deformation effect suggests that current contact models used in dynamics simulations can use the contact stiffness obtained from hysteresis loops as long as the contact interface is not fully discretised, in order to account for the missing bulk deformation information. By contrast, when the interface is more accurately discretised, the stiffness obtained from the ultrasound is the most suitable.

It was also observed that an asymptote in the reflection/transmission appeared at large normal loads. This is a plastic phenomenon that does not necessarily follow a continuous trend, but plateaus appear after the first loading cycles, having a potential impact for dynamic computations and experiments for engineering applications, where often the first loading effects are not taken into consideration and a constant tangential contact stiffness is assumed.

5. Vibration tests under varying sliding conditions and fixed normal load

This campaign aims at assessing the feasibility of the ultrasound technique to detect stick, microslip and gross slip regimes at the contact interface during oscillating motion. For this purpose, hysteresis loops were recorded at varying displacement amplitudes, while ultrasound bursts were simultaneously sent to the contact interface. The normal load was kept fixed at 100 N, which enabled the observation of a wide range of displacement amplitudes. Before starting the experimental campaign, specimens were run on the friction rig for 5 h at 30 μm of displacement amplitude in order to reach a steady-state contact behaviour due to wear since it has been shown that contact interfaces only stabilise when the wear is fully extended over the whole contact [4,21]. Ultrasonic tests started then at a hysteresis displacement of 30 μm, which was stepwise reduced to 0.4 μm, and then increased again to check for the repeatability (see the loading sequence in Table 2). Note that, at the voltage levels used in this study, the displacement amplitudes induced by the ultrasonic waves are in the nanometer range, which is two orders of magnitude lower than the displacement amplitudes of the measured hysteresis loops. Therefore, ultrasonic waves are not expected to perturb the hysteresis measurements at 100 Hz. This was confirmed by acquiring hysteresis loops with and without ultrasonic waves, and observing that they always retained the same hysteretic shape.

5.1. Hysteresis loop measurements

A typical set of measured hysteresis loops is shown in Fig. 11a. When the displacement amplitude is small, hysteresis loops are in the stuck regime, and as the displacement increases, they gradually enter microslip and eventually gross slip. For each displacement amplitude, 10 consecutive loops were recorded, and the contact stiffness was estimated for each loop from the gradient of the stick portion, considering the part from the point of motion reversal up to the 0 N friction force, as shown in Fig. 1. Fig. 11b shows the mean contact stiffness extracted with this procedure, with each error bar indicating two

Table 2
Summary of test loading conditions for the tests under different displacement amplitudes and constant normal load.

Test conditions	Static normal load [N]	Displacement amplitude [μm]
Room temperature 9 mm^2 flat nominal area of contact 100 Hz harmonic excitation 304 Stainless steel specimen	100	30, 25, 20, 15, 10, 5, 4, 3, 2, 1, 0.4, 1, 2, 3, 4, 5, 10, 15, 20, 30

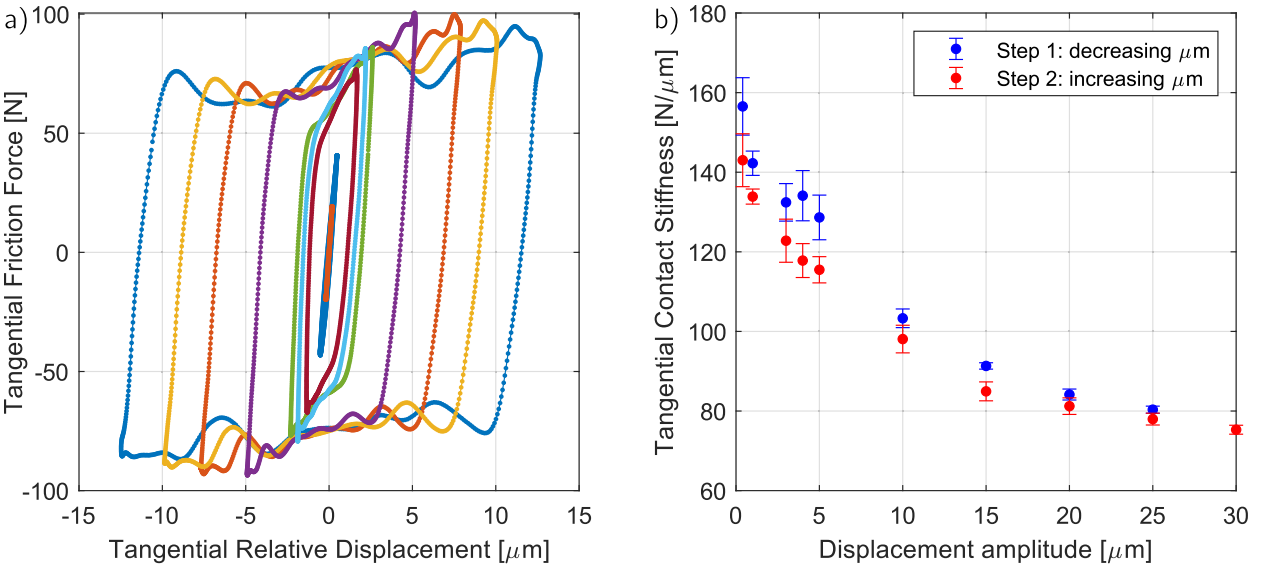

Fig. 11. Tests under different displacement amplitudes and constant normal load: (a) Hysteresis loops; (b) k_t, tangential contact stiffness extracted after load reversal for each hysteresis loop.

times the standard deviation (i.e. 95% of the values) of the 10 consecutive hysteresis loops measured at each normal load. Interestingly, the contact stiffness reduces by approximately 50% over the sixtyfold increase in displacement amplitude, nearly reaching an asymptote at the largest tested amplitude. It has to be noted that this is the contact stiffness estimated right after load reversal, and has not to be confused with the "instantaneous" stiffness, which also decreases with increasing displacement amplitude, and becomes zero during gross slip (when the hysteresis loop shows a horizontal line). The drop in the tangential contact stiffness (evaluated after load reversal) with the increasing displacement amplitude has been observed in few previous studies [64,65,4,66], but no physical explanation has been provided so far.

A hypothesis is proposed here to explain this behaviour via the junction growth phenomenon introduced by Tabor [67] and via the so-called ageing that dates back at least to Rabinowicz [68]. Tabor [67] postulated that when a normal or tangential load is applied onto two contacting interfaces, growth in the real area of contact occurs to accommodate that load. At the beginning of the contact, the real contact area is infinitesimal and consequently, the pressure is almost infinite at the asperity tips. The high pressure leads to plastic deformation at the tips, with a consequent increase in the real area of contact until the pressure drops below the yield stress of the material. Tabor [67] showed that this phenomenon is plastic since, in the tests of his referenced studies, the contact stiffness increased during the first tangential loading, but when the load was reduced again, the contact stiffness remained the same, thus confirming that a plastic hardening had occurred together with a permanent increase in the area of contact. The junction growth phenomenon is here applied to the sliding contact to explain the decrease in the contact stiffness with the increasing displacement amplitude. In the case of stick loops, the tangential load is repeatedly applied on the same asperities, which hence can undergo the junction growth during the first cycle, but during subsequent cycles no further change to the contact interface will occur. This will lead to an increase during the first cycle in the tangential contact stiffness (which is normally not observable due to the start-up of the rig), which then stays constant over the following cycles. On the contrary, in cases of larger displacement amplitudes, new sets of asperities get in contact for the first time during the stick section of each loop, since the specimen has travelled long distances in gross slip before entering the stick state again. Since these new asperities have not undergone the junction growth yet, the overall observed contact stiffness in the stuck part of the hysteresis loop has a lower value. This plastic phenomenon is similar to the flattening of the asperities already described in Section 4.2, which led to the asymptotic behaviour in the contact stiffness after the first plastic loading. Several other studies support this hypothesis. For example, Kendall and Tabor [45] observed

an increase in the ultrasonic transmission with the tangential load and suggested that the transmission increased because of an increase in the real area of contact due to the junction growth. Courtney-Pratt and Eisner [69] also confirmed the same behaviour using electrical resistance measurements, while Ovcharenko et al. [14] confirmed the same behaviour with optical measurements to access the real area of contact.

In addition to this phenomenon, the junction size at the asperity contact also depends on the so-called ageing, namely the time of stationary contact during which the contact size increases, probably induced by asperity creep and strengthening of bonding at asperity contacts [68,70–72]. Optical measurements have in fact shown how the real area of contact slowly increases, typically logarithmically, with the time spent in contact, at rest, due to the ageing or contact rejuvenation [16,19]. This concept can be applied to the present measurements by assuming that the stick condition is equivalent to a period of stationary resting contact. In fact, the ageing would lead to increased stiffness values during repeated (quasi-stationary) stick cycles at low displacement amplitudes (without any gross slip that would instead refresh the contact). On the contrary, at large displacement amplitudes, the asperities would be in stick conditions (i.e. a quasi-stationary contact) for shorter periods of time, thus reducing the amount of ageing and consequently resulting in a lower contact stiffness. This hypothesis is also well supported by a recently published work from some of the authors [46], which reported ultrasonic tests performed during stick cycles where an increase in the contact stiffness was observed after an ageing-induced junction growth due to the repeated loading of the contact at the low displacement amplitudes with no gross slip.

Finally, it is worth mentioning that, at large excitation frequencies, dynamic effects such as self-excited vibrations could affect the measurement of hysteresis loops. Nevertheless, in a previous study performed on the employed friction rig [52], the frequency characteristics of the friction force were investigated, and it was shown that the dynamic effects are minimised when 100 Hz excitation is used to excite the rig. Additionally, other studies suggested that a chaotic behaviour might appear during dynamics experiments [73], although the hysteresis measurements obtained in this work appeared to be unaffected by such behaviour since they exhibited high stability and repeatability during the whole testing campaign.

5.2. Mean ultrasound values: dependence on the displacement amplitude

100 ultrasound bursts were sent within each hysteresis loop over the 10 consecutive loops, resulting in 1000 bursts, in analogous fashion as already described in Section 4.2. Transmission and reflection were recorded, and since they showed equal and opposite trends, only the transmission is presented here. Fig. 12a shows the 1000 maxima of the transmitted signals at different displacement amplitudes, providing a series of interesting new insights into the mean signal values (described in this section) and their variability (described in the next section).

Fig. 12a shows that the mean transmitted signal decreases with the increasing displacement amplitude. Following the previously introduced hypothesis of reduced junction growth and ageing, the larger displacement amplitude leads to a lower contact stiffness and consequently to reduced transmission. The trend is better seen in Fig. 13, which plots the evolution of reflection and transmission as a function of the displacement amplitude where the error bars indicate the 95 percentiles of the 1000 ultrasound bursts maxima. The reflected signal follows the opposite trend of the contact stiffness evaluated from the hysteresis loops (see Fig. 11b), while the transmitted signal follows a similar trend as the contact stiffness since the drop in the stiffness due to the reduced junction growth and ageing leads to more reflection and less transmission. This ultrasonic dependency on the displacement amplitude is a novel observation that shows how ultrasonic measurements can be used to identify the contact condition at the interface.

Once the reflected signal was recorded, the tangential contact stiffness was estimated from Eq. 1 by using reflection coefficients obtained with Eq. A.1 for different displacement amplitudes. The reference maximum value, V_{max}, needed in Eq. A.1 to estimate the reflection coefficient, was obtained from the test at 0 N normal load (i.e. no contact) from the previously shown measurements in stuck vibration. Detailed results of the contact stiffness are not shown here since they follow the same behaviour of the contact stiffness obtained from hysteresis loops, as discussed in Sections 4.2 and 4.3. However, a comparison plot is shown in Fig. 14a, showing the relationship between the k_t from the hysteresis loops and the k_{us} from reflection (obtained by multiplying K_{US} by 9 mm^2). The slope of the best linear fit is very similar to that shown in Fig. 9a, suggesting that the same physical dependency holds when either changing the normal load or the displacement amplitude. Likely, this is again driven by changes in the number and size of contact spots and overall real area of contact due to the varying loading. Similarly to what presented with Fig. 9b, a comparison is also provided between the k_t from the hysteresis loops and the ultrasound transmission in Fig. 14b, showing that a linear relationship still exists between the two. The values of transmission are the mean values of the 1000 bursts. Although the slope is larger than that in Fig. 9b, the linear relationship still holds, even in the case of gross slip, confirming the strong correlation between contact stiffness and ultrasonic transmission.

5.3. Variations in the ultrasound measurement: effect of friction regimes

Fig. 12a shows a large variability over the 1000 bursts as the displacement amplitude increases. Peaks and valleys appear around the mean transmission as the hysteresis loops go from the stick to the gross slip regime. There are almost no variations for the full stick case, while in the microslip and gross slip regimes the variations are on the order of 0.2 V and 0.4 V, respectively. A closer inspection reveals that there are two peaks and valleys per hysteresis loop. This ultrasound behaviour

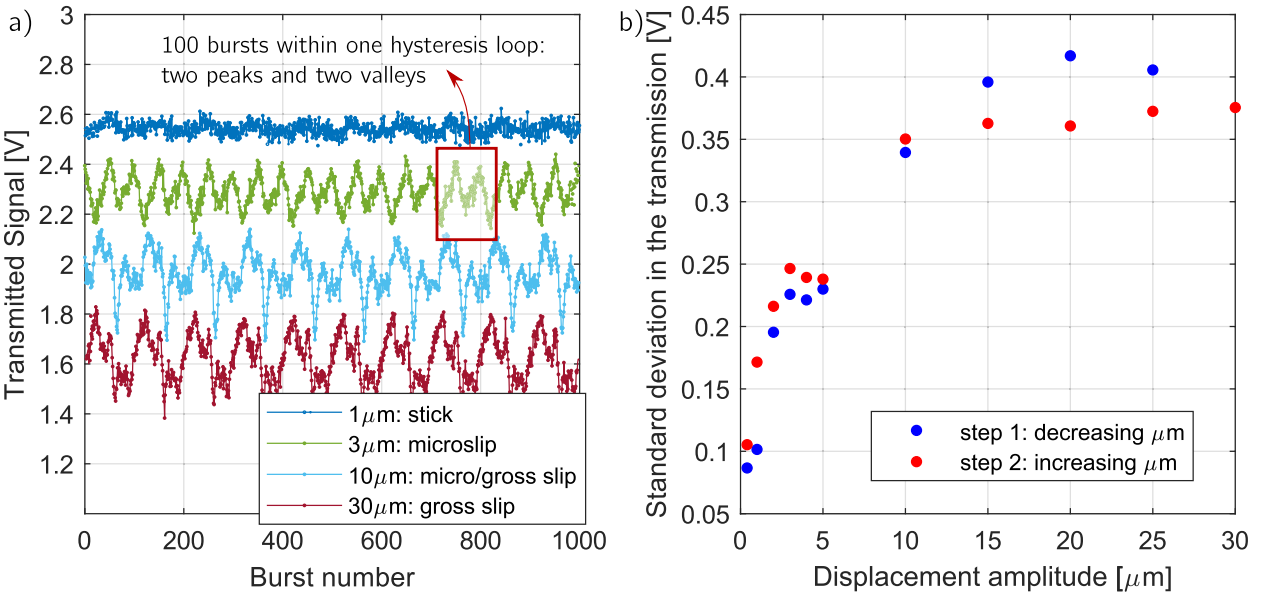

Fig. 12. Tests under different displacement amplitudes and constant normal load – transmitted signal within hysteresis loops: (a) Time history of the transmission within 10 consecutive hysteresis loops measured at different displacement amplitudes; (b) Standard deviation from mean transmission within the hysteresis loops measured at different displacement amplitudes.

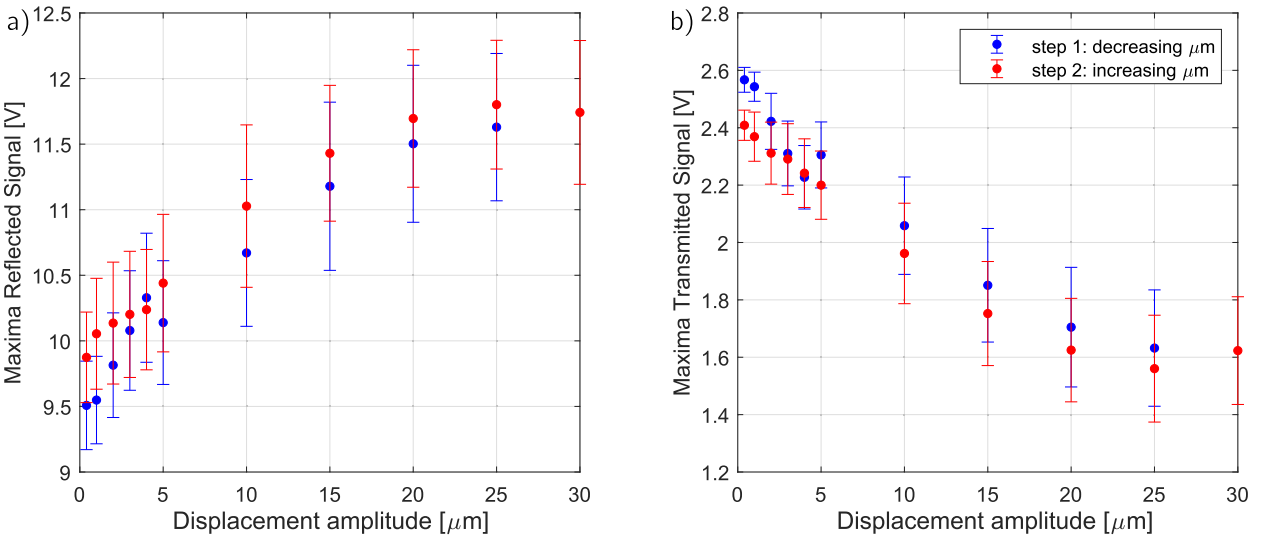

Fig. 13. Tests under different displacement amplitudes and constant normal load: (a) Reflected and (b) Transmitted signals as a function of the displacement amplitude.

has never been reported before, and this novel observation suggests that the ultrasound variability in the transmission depends on the contact condition at the interface and consequently may be used to detect stick–slip changes at the contact.

Fig. 12b quantifies this observed variability (i.e. the average signal variation in the transmitted signal) by plotting the standard deviation of the 1000 bursts. The variability increases with the displacement amplitude of the hysteresis loops, and it seems to reach a stable value for loops with more than 10 μm displacement amplitudes. It is interesting to note that 10 μm (±5 μm) is the threshold displacement amplitude after which the loops enter in gross slip as shown in Fig. 11a, suggesting that the variation in the transmitted signal is (a) indicative of the ratio between stick and sliding states at the contact, and (b) constant once the full contact enters in gross slip. In addition, the standard deviation in Fig. 13b increases with the displacement amplitude (note that the standard deviations reported in 13b are the same quantities shown in Fig. 12b). An analogous trend exists in Fig. 13a, although less evident because the ultrasound reflection is affected by other sources of noise as described in Appendix A. This large variability has not been observed in the two previous studies in which ultra-

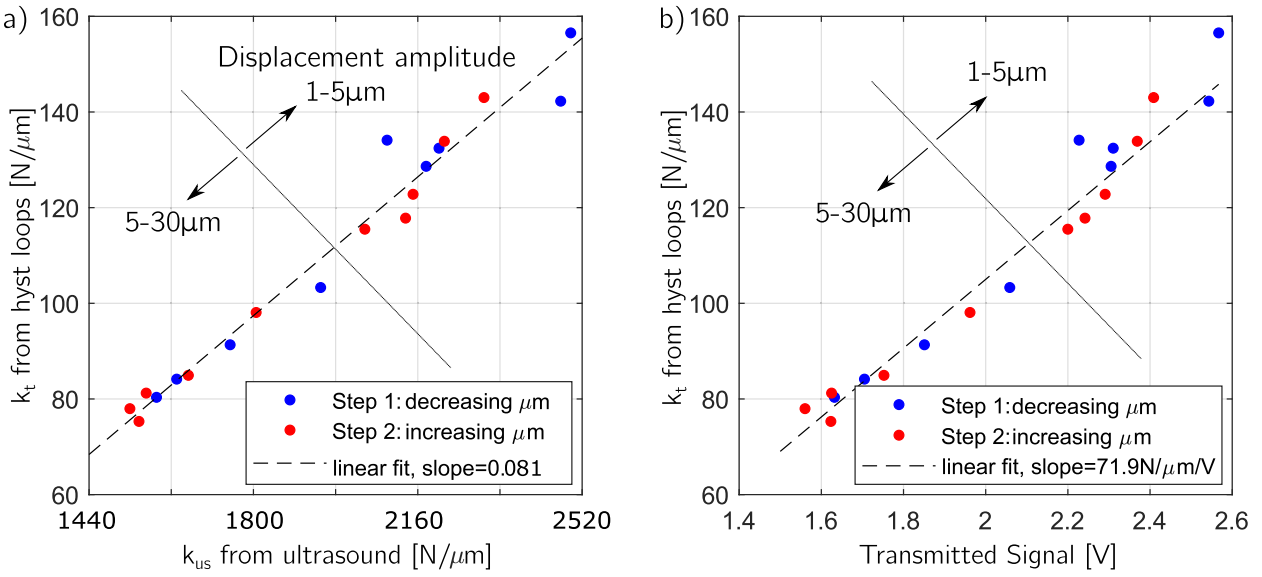

Fig. 14. Tests under different displacement amplitudes and constant normal load – each point corresponds to different hysteresis loops with different displacement amplitudes: (a) k_t from hysteresis loops vs k_{us} from ultrasound reflection; (b) k_t from hysteresis loops vs transmitted signal.

sound signals were acquired simultaneously with hysteresis loops [38,46]. Mulvihill et al. [38] observed a constant reflection over the hysteresis loop, probably due to the quasi-static nature of their tests and relatively small displacement amplitudes of only 2.5 μm. Pesaresi et al. [46] only used one ultrasound burst for each loop, thus making it difficult to draw any valid conclusion about variability within a loop.

To better understand the physical origin of the observed variability, Fig. 15a plots the four different time histories from Fig. 12a on top of the respective hysteresis loops. The amplitude of the transmitted signal is shown as a colour variation to easily allocate the position of the peaks/valleys along the loops and help with their interpretation. Colorbars with the same range of variation of 0.4 V are used for the 4 loops, centred around each mean so that the colour change can be used as an indication of the actual variability within the loop. The ultrasound transmission is also plotted as a function of the relative displacement in Fig. 15b. Based on these plots the following observations for the three friction regimes were made:

Stick regime (1 μm):

The transmission is mostly constant over the loop, as confirmed by Figs. 15b and 12a. The observed small variability is probably due to the measurement noise. This agrees with the time histories of loops measured at 0.4 μm from Fig. 6b).

Microslip regime (3 μm):

Peaks in the transmission appear at the beginning of the stick region, followed by subsequent drops as microslip occurs. This suggests that when the contact is slowly approaching the stuck condition, the conformity increases due to the ageing of the junctions, and hence the signal is transmitted to a larger extent. As soon as microslip starts, new asperities without any conformity attributed to the ageing enter in contact, while previously conformal asperities separate, and as a consequence the transmission drops. As the motion is about to be reversed again (slightly before the beginning of stick), the tangential load is large (slightly lower than the friction limit) and a new junction growth occurs on the asperities in contact at that moment, thus leading to the peak in transmission at the beginning of the stick phase. The two peaks and valleys in the transmission are visible in Figs. 15a and 12a and lead to V-shaped transmission curve in Fig. 15b for the case at 3 μm displacement, where the two peaks correspond to the stick region, and the central drop corresponds to the microslip region. The junction growth and ageing hypotheses, here used to explain the observed increase during stick and the decrease at the onset of slip/microslip, are strongly supported by optical measurements of the evolution of the real area of contact under shear loading [16,18]. Those studies confirm that the real area of contact (and indirectly the contact stiffness) slowly increases at rest through ageing and drops at slip inception since already aged microjunctions gradually slip and are replaced by new, smaller microjunctions. Drops in the area of contact observed on those studies were as large as few tens percent with respect to their respective mean values, which are of the same order of magnitude as the drops in transmission observed here (17% for the 0.4 V drop over the 2.3 V mean value shown in Fig. 15b in the 3 μm case). It is worth noting that the above-mentioned studies only investigated transparent and soft materials because of the limitations of optical measurements. Here, instead, opaque steel is used, hence revealing for the first time such evidence for a metallic material.

Gross slip regime (10 and 30 μm):

A strong asymmetry of the transmitted signal is evident in Fig. 15a between the top friction limit of the loop and the bottom one. The transmission at the top friction limit is 0.2 V higher than the average, while in the bottom friction limit it is 0.2 V lower. This dominant asymmetry was not attributed to contact states but was linked to a normal load variation in

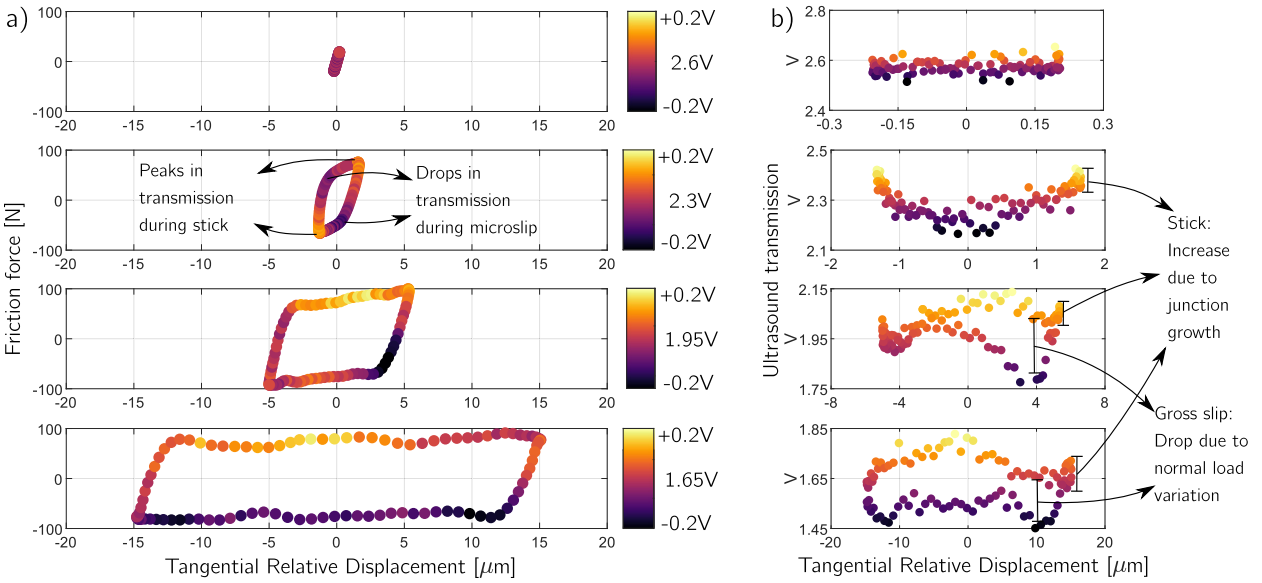

Fig. 15. (a) Ultrasonic transmission (in colorbar) within the hysteresis loops measured at different displacement amplitudes (1, 3, 10 and 30 μm respectively). The respective ultrasound time histories are shown in Fig. 12a; (b) Ultrasonic transmission plotted versus the relative displacement to better identify peaks and drops.

the test rig, caused by the kinematics/dynamics of the rig when it moves along the two different sliding directions. Fig. 7b shows that a transmission variation of ±0.2 V around the 100 N value would correspond to a ±30 N normal load variation. Therefore, according to this hypothesis, the +0.2 V variation is associated to a 130 N (100 N plus 30 N) normal load acting on the top friction limit, while the −0.2 V variation is associated to a 70 N (100 N minus 30 N) normal load on the bottom friction limit. This indicates that when the contact slides in one direction it has a lower normal load than when it slides in the opposite direction. This hypothesis found confirmation via the analysis shown in Appendix C, which shows a simplified FE structural simulation of the bending exerted on the friction rig as a result of the application of a tangential excitation. The simulation shows that the bending resulting from the tangential excitation leads to a state of tension or compression at the contact depending on the direction of excitation. This tension or compression state at the contact is superimposed to the nominally applied compressive static normal load. The superimposed tension/compression is estimated at roughly the 13% of the applied tangential load. In the hysteresis loops examined in this section, the applied tangential load is roughly 100 N in the two sliding directions, thus resulting in an increase in the normal load of 13 N in one sliding direction, and a decrease of 13 N in the other direction. While this estimated value of 13 N is lower than the ultrasonically estimated change of 30 N normal load in the two friction limits, the simplified structural simulation confirmed that the bending leads to a state of tension and compression at the contact, which effectively changes the normal load in the two sliding directions.

It must be noted here that the above observations should result in two different friction limits, μN_0, given that they are directly proportional to the normal load, N_0, and assuming a constant friction coefficient, μ, over the loop. However, very similar friction limits in the measured hysteresis loops are observed at around 100 N (positive and negative) in the last plot in Fig. 15a. A possible explanation for this symmetric friction limit behaviour is attributable to the dynamic load transducers that measure the friction force. These transducers are designed to measure fast variations around a mean value and consequently cannot pick up steady offsets. The 30 N offset, generated by the normal load variation, acts as a constant value over the loop (the loop is shifted upwards by a 30 N offset), and consequently cannot be picked by the transducers. In fact, the transducers re-centre the loop around 0 N, effectively filtering out the 30 N offset. Modifications to the test rig will be performed in the future to confirm this hypothesis, but fortunately, this effect does not have a large impact on contact parameter estimations from the hysteresis loops. In fact, the friction coefficient is computed from the absolute distance between the two friction limits, rather than their absolute values. With regards to the contact stiffness, although it is normal load dependent as highlighted by Fig. 5b, the stick regions in the two sliding directions have similar values of ultrasound transmission (see similar colours in the stick regions of the last loop of Fig. 15a), indicating that the normal load is similar in both directions, thus not affecting the two k_t values.

Overlaid to this asymmetry, four peaks are observable in the transmission in loops in gross slip (see Fig. 15b), two major peaks in the centre of the gross slip (top and bottom), and two minor peaks during the initial stick phases. The minor peaks observed at the beginning of the stick region are linked to the junction growth and ageing during the initial stick phase, as already observed in the microslip case at 3 μm. The major peaks in the middle of gross slip are possibly caused by additional changes in the normal load and/or global contact conditions at the interface due to the flexibility of the rig components. In

addition, varying levels of specimen alignments and/or velocity may be responsible for some of the variation, but further refinement of the test setup will be required to confirm these results.

Overall, these results indicate that (a) the highlighted changes observed at the stick–slip transitions are independent of the rig kinematics/dynamics, and, more importantly, (b) the junction growth and ageing behaviours that characterise the stick regime is still detectable in gross slip loops, making it the most promising indicator for slip-stick transitions at the contact interface.

5.4. Summary of vibration tests under varying sliding conditions

The results in this section provide novel insights into the physics of sliding contacts between non-transparent metallic materials. A reduction in the tangential contact stiffness measured from hysteresis loops, after the load reversal, was observed as the displacement amplitude increased. Following the same trend, the ultrasound transmission decreased with the increasing displacement amplitude while the reflection increased accordingly. It is here proposed that this behaviour is linked to a reduced time for the ageing of the asperity contacts as the displacement amplitude is increased. This dependency of the contact stiffness on the displacement amplitude is not commonly accounted for in current contact models for dynamics simulations, but the described stiffness reduction on the order of 50% could have significant implications on the dynamic response and, consequently, updated contact models need to include this effect.

In addition, for the first time the ultrasound transmissibility was recorded at different time instances within a single high-frequency hysteresis loop and a large variability was observed during the vibration cycle. For loops with low displacement amplitudes, i.e. only stick regime, the transmissibility was constant over the whole loop, making the contact indistinguishable from a non-vibrating contact. This suggests that the ultrasound technique cannot be used to determine whether a contact is fully static or is undergoing low amplitude elastic vibrations, at least at these levels of ultrasonic measurement noise. When the displacement amplitude was larger, and microslip and gross slip regimes occurred, peaks in the transmissibility appeared at the beginning of the stick regime (i.e. after the reversal of motion) while the transmission dropped once microslip occurred. The clear detectability of the stick peaks in the transmission highlights the potential for real-time identification of stick and slip transitions in vibrating frictional contacts of non-transparent materials, which are of great interest for industrial applications. For example, vibration tests (similar to traditional nonlinear dynamic testing) can be performed to study complex assembled structures. At first, low-level excitations can be imposed, which would lead to constant transmissibility under stuck conditions. Then, the excitation can be gradually increased, leading to changes in the transmitted signal at larger amplitudes. This would allow detecting for which excitation amplitudes the contact enters microslip/gross slip, thus helping engineers to quantify the damping effect of friction on structures, but also helping to validate the predictions of numerical models used for dynamics simulations. Additionally, refined spatial validations can be achieved by mounting multiple ultrasonic transducers distributed in different regions of the contact area. The use of more transducers would lead to experimental refined grids that can validate the spatially-resolved predictions of the interfaces discretised with FE models. However, this ultrasound technique measures only one variable (i.e. transmission/reflection), thus making it difficult to identify if changes are due to tangential or normal effects or due to wear as discussed in the beginning of Section 5. But, if used in conjunction with hysteresis measurements, it becomes a very powerful tool to accurately characterise the friction mechanisms at the interface and gain physical insights.

Finally, it was also revealed that high-frequency vibratory measurements may lead to static normal load variations that cannot be detected by dynamic load cells, since these exclude any static offset in the recording. This is an important observation for designers and users of high-frequency friction rigs, and the ultrasound technique can be used to monitor such behaviour, thus helping in the correct interpretation of measured data and avoiding erroneous conclusions.

6. Conclusions

This work presents the use of ultrasonic shear waves to investigate the state of a dry metallic friction contact while it undergoes high-frequency shear vibrations. This is achieved by sending multiple ultrasound bursts into a high-frequency oscillating contact interface and acquiring them simultaneously with synchronized hysteresis loop measurements. The interpretation of measurements is aided by the numerical modelling of the ultrasonic wave propagation into the contact.

The results show that the tangential contact stiffness, evaluated from hysteresis loops right after load reversal, strongly correlates with the transmission/reflection of the ultrasonic signal, confirming previously obtained results by other researchers. It is shown that the tangential contact stiffness increases with increasing normal loads, in agreement with previous studies that revealed how this is ultimately due to an increase in the number and size of the individual contact regions. Additionally, it is also found that the contact stiffness strongly decreases with increasing displacement amplitudes of the vibration cycle. This decrease is here attributed to a reduced time for the ageing of the asperity contacts occurring at large displacement amplitudes and should be included in state-of-the-art contact models used for nonlinear dynamic analysis of vibrating jointed structures.

For the first time, a large variability is observed in the ultrasound transmission/reflection amplitude during the vibration cycle. Of particular interest is an increase in the transmissibility at the transition from gross slip to stick, and an opposite reduction at the transition from stick to microslip/gross slip. These variations in the transmissibility were present in all tests

hence representing reliable indicators for the transitions between stick, microslip and gross slip regimes. This suggests that the ultrasonic technique can be used to detect spatially resolved changes in contact states during vibration cycles. This technique has, therefore, the potential to monitor jointed structures in real-time during high-frequency vibrations, thus providing a new powerful tool to gain a fundamental physical understanding of the contact mechanisms in non-transparent engineering materials, and to acquire the missing validation data needed for improved nonlinear dynamic analysis.

CRediT authorship contribution statement

Alfredo Fantetti: Conceptualization, Methodology, Investigation, Writing - original draft. **Stefano Mariani:** Conceptualization, Methodology, Investigation, Writing - original draft. **Luca Pesaresi:** Resources, Writing - review & editing. **David Nowell:** Writing - review & editing. **Frederic Cegla:** Resources, Writing - review & editing, Supervision. **Christoph Schwingshackl:** Resources, Writing - review & editing, Supervision, Funding acquisition.

Declaration of Competing Interest

The authors declare that they have no known competing financial interests or personal relationships that could have appeared to influence the work reported in this paper.

Acknowledgements

A. Fantetti has received funding from the European Union's Horizon 2020 research and innovation program under the Marie Sklodowska-Curie grant agreement No. 721865, project acronym EXPERTISE. The authors are grateful to Prof. Daniele Dini, Head of the Tribology Group in Imperial College London, for the fruitful discussions on the topics of this article and interpretation of the experimental findings.

Appendix A. Finite element analysis to characterize the ultrasonic wave propagation

A finite element model of the specimens was created to characterize the ultrasonic wave propagation in the material. This characterization is needed because, as shown in Section 3.2, the area covered by the shear transducer is larger than the nominal area of contact (see Fig. 3c). This mismatch needs to be considered to correctly estimate the reflection coefficient R at the contact interface, which is required as input in Eq. 1 to obtain the ultrasonically estimated contact stiffness per unit area, K_{US}, since the wave components not directly reaching the area of contact are unaffected by the contact conditions. R can be measured as:

$$R_i = \frac{V_i - V_{min}}{V_{max} - V_{min}} = \frac{V_i - V_{max}/\zeta}{V_{max} - V_{max}/\zeta} \tag{A.1}$$

where V_i is the measured voltage envelope peak in the reflection at any test i in which the specimens are at an unknown compressive contact state, V_{max} and V_{min} are the measured voltage envelope peaks for a fully detached specimen and for specimens in full contact, respectively, and ζ is the ratio between V_{max} and V_{min}. While V_{max} can be obtained simply by measuring the reflection in a single specimen not in contact (since the whole signal would be fully reflected), it is less trivial to measure V_{min}. In fact, V_{min} is different than zero when two specimens are bonded in full contact since part of the waves emitted by the sensor are inevitably reflected back by faces other than the contact interface between the two specimens. Finite element (FE) analyses can be used to estimate the ratio ζ by simulating tests performed on a single specimen and on two fully connected specimens. Such ratio ζ depends fundamentally on the position of the transducer footprint within the specimen and on the geometry of the two specimens. In fact, those two determine (i) the fraction of signal directly reaching the contact area versus the fraction impinging on the other geometrical boundaries of the excited specimen and (ii) the interferences occurring between the various reflected wave components as they travel towards the sensor. Once ζ is estimated, V_{min} can be substituted by V_{max}/ζ in Eq. A.1, so that the reflection coefficient can be obtained by experimentally measuring V_i, and then used in Eq. 1 to estimate the contact stiffness from ultrasound.

Simulations were performed with Pogo, which is a well-suited software to solve wave propagation problems involving a large number of elements [74]. A 3D model of the two specimens in full contact (Fig. 16a) was generated using linear tetrahedral elements with edges of 0.05 mm nominal length (~23 M elements in total). This model is referred to as "model with bonded contact". Care was taken to form a smooth boundary at the interface between the two specimens (i.e. impeding element faces from crossing it), so that a single specimen model could be simply obtained by deleting the bottom specimen elements. The single specimen is referred to as "model with no contact". To reach the required accuracy, it is generally recommended to include at least 20 elements per shortest propagating wavelength [75]. In this model, 30 elements are offered to discretize a 2 MHz shear wavelength, hence safely meeting the accuracy requirement. For stability, the Courant-Friedrichs-Lewy condition dictates that the fastest wave-front must not travel more than one element in a single time-step [76]. The fastest waves that propagate through the model are longitudinal waves, which are generated alongside the input shear waves due to the finite extent of the transducer active surface and due to mode-conversion of shear waves

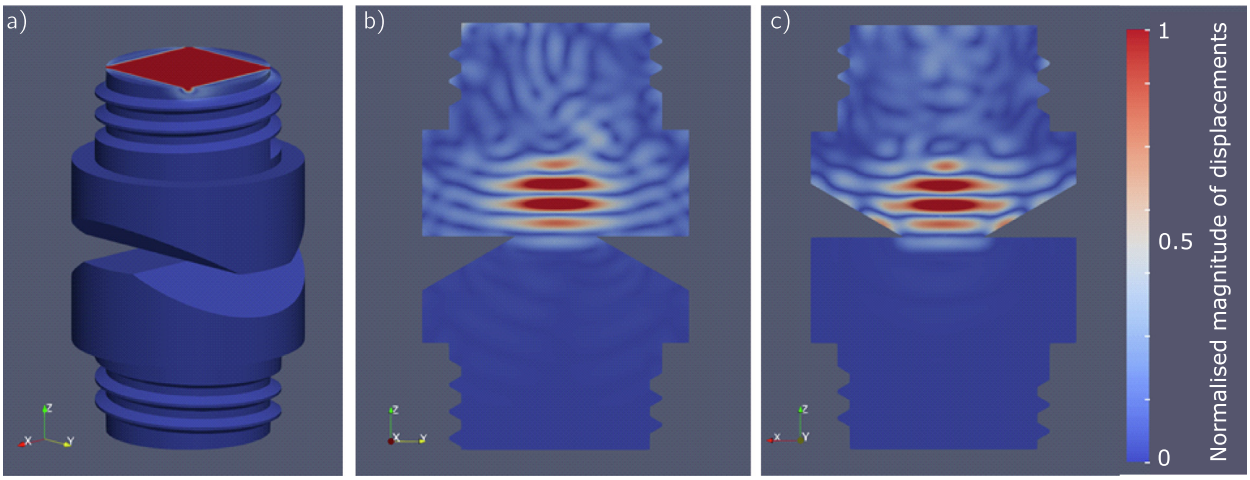

Fig. 16. Colour-coded magnitude of displacements measured at two simulation times for the "bonded contact model". (a) At 0.25 μs the sensor is exciting the shear wave polarized in the y-direction. The red area in the figure shows the extent of the modelled sensor patch. (b)–(c) Section cuts in the y-z and z-x planes, respectively. At 3 μs part of the shear wave has entered the bottom specimen. However, a portion of the wave is being reflected from other geometrical boundaries of the top specimen and is directed back towards the sensor. (For interpretation of the references to colour in this figure legend, the reader is referred to the web version of this article.)

reflected from the specimen boundaries; by setting the simulation time-step to 1 ns a longitudinal wave travelling at about 5.7 km/s takes more than 8 time-steps to travel through a single element, hence safely satisfying the stability condition.

The actuator stage of the transducer was modelled by applying a shear force, in the y-direction, to the nodes lying within the footprint of the actual piezoelectric surface on the top surface of the top specimen, as shown in the red square patch of Fig. 16a. Similarly, the wave sensing stage was simulated by averaging the displacements measured on the same nodes at each simulation time. The grade 304 steel was modelled as an isotropic medium, whose material properties were first assigned within the ranges of values found in literature and then refined by comparing the results from the "no contact" model to an experimental signal acquired on a single specimen (Fig. 17a). This process resulted in setting a density of 8000 kg/m^3, an elastic modulus of 193 GPa and a Poissons ratio of 0.29, for which a satisfactory agreement between experimental and simulation results was obtained, as seen in Fig. 17a. Note that a perfect match between the two signals can hardly be obtained, since the exact RF shape of the wave transmitted by the actual sensor is inevitably different than the supplied voltage excitation signal, due to the specific "transfer function" exerted by the sensor assembly and the bonding adhesive, which is difficult to measure experimentally [77].

Fig. 16b and c display the magnitude of displacements measured after 3 μs of simulation time for the model with bonded contact on two section cuts passing through the middle of the specimens either (b) in the direction of shear polarization (side view in Fig. 3c) or (c) in the orthogonal direction (front view in Fig. 3c). As seen in the figures, the largest fraction of shear wave amplitude is effectively directed towards the interface between the two specimens, with a wave-front essentially parallel to the interface itself; also, at 3 μs the first part of the excited tone burst has already entered the bottom specimen. However, a smaller fraction of shear amplitude hits the lower boundary of the top specimen outside the contact patch, from which it is totally reflected towards the top sensor active surface (except for negligible losses into the air). The various reflected components interfere within each other and arrive at the transducer at slightly different times depending on the exact length of the travelled path, producing the black signal of Fig. 17b. This contribution to the actual received voltage was already defined V_{min} in Eq. A.1 and is virtually unaltered at any compressive contact state. By contrast, in the model with no contact the shear wave impinging on the contact patch is entirely reflected back towards the sensor (again, excluding negligible losses into the air) producing the red signal in Fig. 17a and b. Note that in Fig. 17b both signals are normalized to unity at the peak of the red envelope, and the ratio between the predicted peaks of the "no contact" and "bonded contact" model envelopes is $\zeta = 4.5$.

As explained above, this estimated value of ζ can be used to compute the reflection coefficient R_i that characterizes any test in which the specimens are at an unknown compressive state via Eq. A.1, i.e. by using the measured voltage envelope peak V_i and by expressing V_{min} as a function of V_{max}, which can be readily measured by testing a single specimen before pressing the specimens in contact to each other. Clearly, V_i will represent an "averaged" indication of the contact condition over the entire contact patch, since the wave front reaching the interface is larger than the interface itself, as seen in the FE solutions of Fig. 16b and c. The estimated R_i can then be used in Eq. 1 to compute the ultrasonically estimated contact stiffness per unit area, K_{US}, for the entire contact patch.

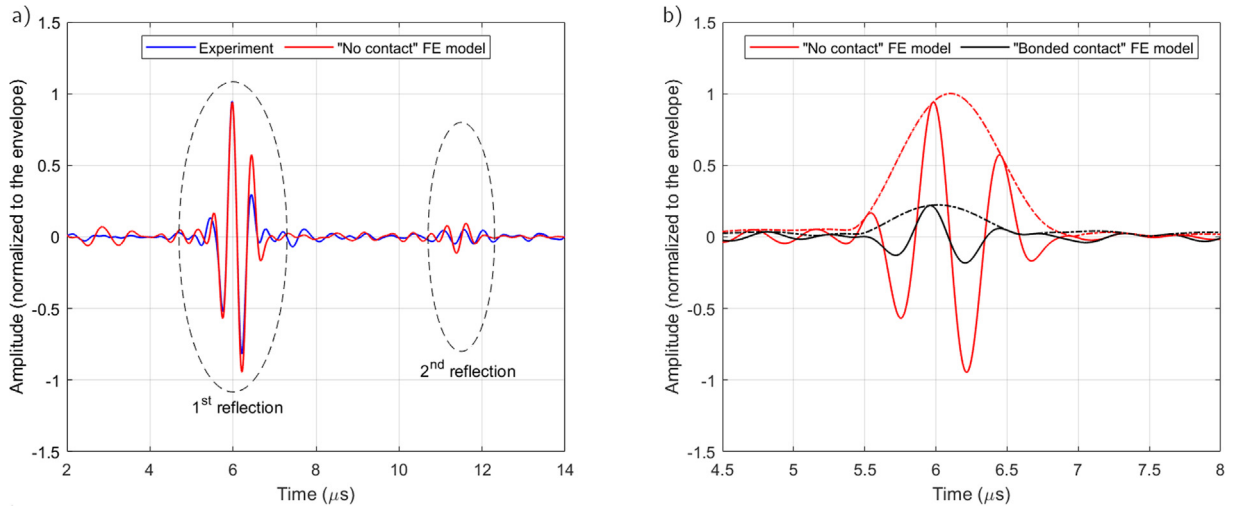

Fig. 17. a) Comparison between experimental and numerical signals obtained for the "no contact model" (both signals normalized to the peak of their envelopes). (b) Comparison between numerical signals obtained for "no contact" (same as red signal in (a)) and "bonded contact" models, both signals being normalized to the envelope peak of the former. (For interpretation of the references to colour in this figure legend, the reader is referred to the web version of this article.)

Appendix B. Finite element analysis to estimate the specimen tangential bulk deformation

A finite element model of the specimens was created to estimate the specimen bulk deformation induced by applied tangential loads. The bulk deformation is needed to quantify the difference between the contact stiffness obtained from ultrasound measurements, which only include the interface compliance, and that obtained from hysteresis loops, which also include the bulk deformation in addition to the interface compliance.

The same 3D model of the specimens shown in Appendix A was used to replicate the experimental tangential loading. In this way, it was possible to estimate the compliance between the two points shown in Fig. 18a, which correspond to the experimental location of the laser points used to measure the relative displacement of the hysteresis loop. Since the specimen FE models have perfectly flat and fully bonded interfaces, the relative displacement between the two highlighted points only gives the compliance due to the bulk deformation of the specimens, while the compliance due to the interface is null (i.e. infinite stiffness of the bonded contact). After estimating the bulk deformation contribution from the FE model and its corresponding stiffness, k_{bulk}, Eq. 3 can be used to superpose k_{bulk} to the stiffness obtained ultrasonically, for better comparison against that extracted stiffness from hysteresis measurements.

The 3D specimens model was imported in Solidworks and re-meshed using linear tetrahedral elements with an average size of 0.5 mm (~70 k elements in total). A static tangential load was applied on the top surface of the top specimen. The thread of the bottom specimen was constrained in all degrees of freedom, while the top specimen was only allowed to move along the direction of excitation to best replicate the rig operating conditions. By dividing the applied load by the relative displacement between the two points of displacement measurement, the stiffness solely due to the bulk deformation is obtained. Fig. 18b shows the bulk stiffness between different locations. As the point distance increases, the stiffness decreases since the relative tangential displacement is larger. The mid-points are those closer to the real laser measurement points, and they result in a bulk stiffness value of 361 N/μm, which is used in Section 4.3 for the comparison between contact stiffness values obtained from ultrasound and hysteresis measurements.

Appendix C. Finite element analysis to estimate the normal load variation due to the bending of the arms

As mentioned in Section 5.3, ultrasonic measurements suggested that a strong normal load variation occurs when the friction rig enforces motions in the two opposite sliding directions. To investigate this aspect, a simplified structural model of the friction rig was created in Abaqus, as shown in Fig. 19a. The model represents the moving and static arms by means of Beam elements made of stainless steel material. The moving arm is free to move horizontally and is constrained with a hinge at its right side to simulate the free rotation due to the knife edge (a detailed description of the friction rig can be found in [52]). On its left side, the moving arm is connected to the static arm by means of the clamped specimens. The top push rod, which transmits the normal load, is hinged in both directions (on the top, where it is connected to the pneumatic actuator, and on the bottom, where it is connected to the moving arm). The static arm is grounded at the dynamic load cell locations and it is also connected to the hinged bottom push rod. Fig. 19b-c show the rig deformation after the application of a 100 N tangential load that acts on the location corresponding to the actual axis of the shaker excitation. Clear bending motions/

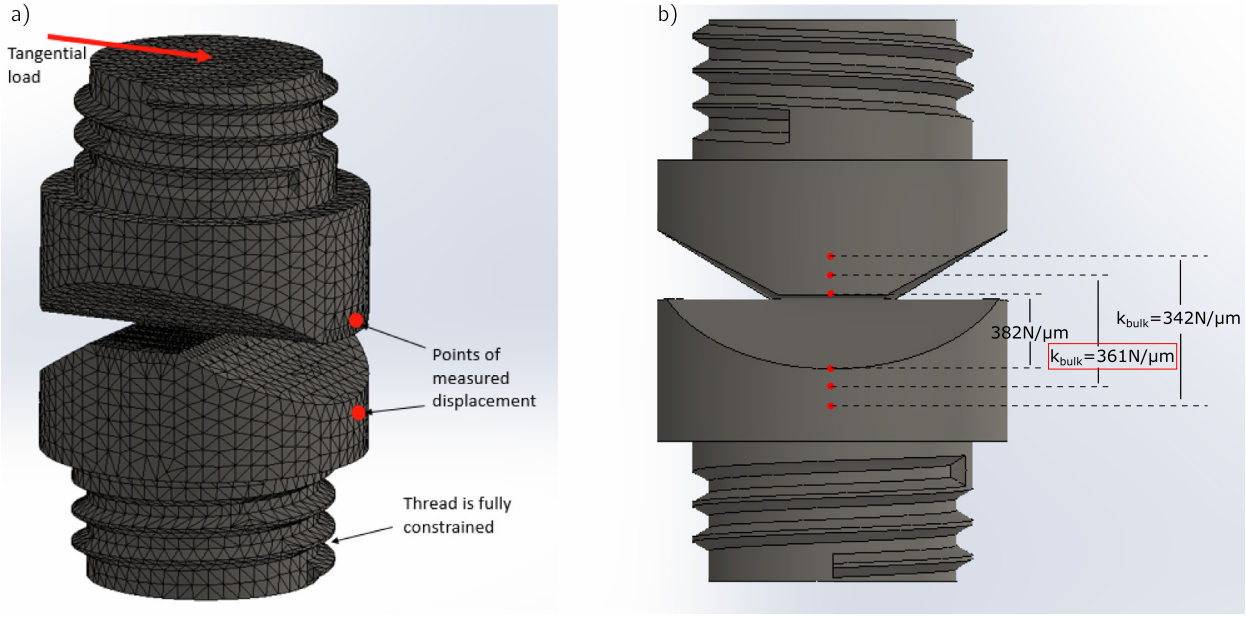

Fig. 18. (a) FE mesh of the specimens and points of measured displacement; (b) Bulk stiffness values at different locations. The further apart the measurement points, the lower the bulk stiffness, k_{bulk}.

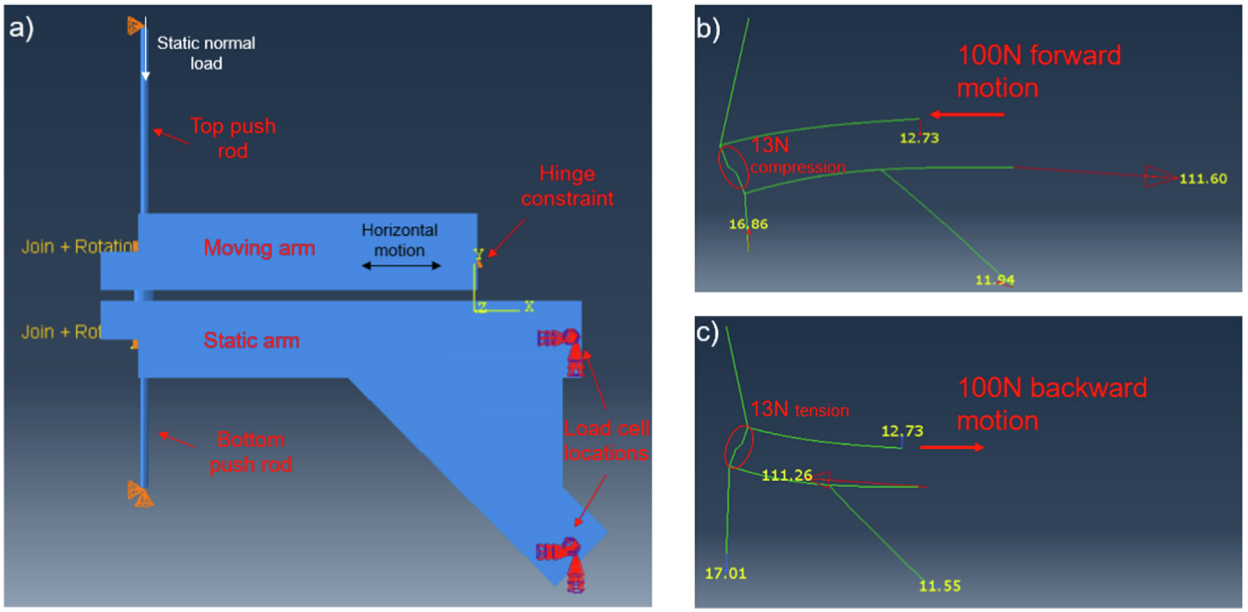

Fig. 19. (a) Simplified structural model of the friction rig; (b) Compression at the contact resulting from a tangential load of 100 N pushing forward; (c) Tension at the contact resulting from a tangential load of 100 N pulling backward.

stresses are observable, as expected, since the excitation force is on a different axis than the opposite reaction forces on the static arm load cells, and therefore a moment is generated. This moment generates bending, but more importantly it generates a compressive force in the contact between the specimens when the moving arm moves forward (going to the left and downward as in Fig. 19b, and conversely, a tension when the moving arm moves backward (going to the right and upward as in Fig. 19c). The tension at the contact appears since specimens are pulled backwards and tend to open. The compression and tension resulting from the applied 100 N tangential load are both estimated at 13 N, as shown in Fig. 19b and c. This corresponds to a 26 N normal load difference at the contact when the rig moves in the two opposite directions (i.e. 26% of the tangential load), hence partially confirming the conclusions drawn from the ultrasonic measurements described in Section 5.3.

References

[1] M.R. Brake, The Mechanics of Jointed Structures: Recent Research and Open Challenges for Developing Predictive Models for Structural Dynamics, Springer International Publishing, 2018.
[2] L. Gaul, R. Nitsche, The role of friction in mechanical joints, Appl. Mech. Rev. 54 (2) (2001) 93, https://doi.org/10.1115/1.3097294, URL:http://appliedmechanicsreviews.asmedigitalcollection.asme.org/article.aspx?articleid=1555301.
[3] G. Kerschen, K. Worden, A.F. Vakakis, J.-C. Golinval, Past, present and future of nonlinear system identification in structural dynamics, Mech. Syst. Signal Process. 20 (3) (2006) 505–592, https://doi.org/10.1016/j.ymssp.2005.04.008, URL:http://linkinghub.elsevier.com/retrieve/pii/S0888327005000828.
[4] A. Fantetti, L. Tamatam, M. Volvert, I. Lawal, L. Liu, L. Salles, M.R. Brake, C. Schwingshackl, D. Nowell, The impact of fretting wear on structural dynamics: experiment and simulation, Tribol. Int. 138 (2019) 111–124, https://doi.org/10.1016/j.triboint.2019.05.023.
[5] M.R. Brake, C.W. Schwingshackl, P. Reuß, Observations of variability and repeatability in jointed structures, Mech. Syst. Signal Process. 129 (2019) 282–307, https://doi.org/10.1016/j.ymssp.2019.04.020.
[6] M. Krack, L. Salles, F. Thouverez, Vibration prediction of bladed disks coupled by friction joints, Arch. Comput. Methods Eng. 24 (3) (2017) 589–636, https://doi.org/10.1007/s11831-016-9183-2.
[7] R. Lacayo, L. Pesaresi, J. Gross, D. Fochler, J. Armand, L. Salles, C.W. Schwingshackl, M.S. Allen, M.R. Brake, Nonlinear modeling of structures with bolted joints: a comparison of two approaches based on a time-domain and frequency-domain solver, Mech. Syst. Signal Process. (114) (2019) 413–438..
[8] E.P. Petrov, D.J. Ewins, State-of-the-art dynamic analysis for non-linear gas turbine structures, Proc. Inst. Mech. Eng. G J. Aerosp. Eng. 218 (3) (2004) 199–211, https://doi.org/10.1243/0954410041872906.
[9] C.M. Firrone, S. Zucca, Modelling friction contacts in structural dynamics and its application to turbine bladed disks, Numer. Anal. Theory Appl. (2011) 301–334, https://doi.org/10.5772/25128, URL:http://www.intechopen.com/books/numerical-analysis-theory-and-application/modelling-friction-contacts-in-structural-dynamics-and-its-application-to-turbine-bladed-disks%0Ahttp://www.intechopen.com/books/numerical-analysis-theory-and-application.
[10] C. Gastaldi, M.M. Gola, On the relevance of a microslip contact model for under-platform dampers, Int. J. Mech. Sci. 115–116 (2016) 145–156, https://doi.org/10.1016/j.ijmecsci.2016.06.015, URL:https://doi.org/10.1016/j.ijmecsci.2016.06.015.
[11] L. Pesaresi, J. Armand, C.W. Schwingshackl, L. Salles, C. Wong, An advanced underplatform damper modelling approach based on a microslip contact model, J. Sound Vib. 436 (2018) 327–340, https://doi.org/10.1016/j.jsv.2018.08.014.
[12] L. Panning, W. Sextro, K. Popp, Spatial dynamics of tuned and mistuned bladed disks with cylindrical and wedge-shaped friction dampers, Int. J. Rotat. Mach. 9 (3) (2003) 219–228, https://doi.org/10.1080/10236210390147308.
[13] J. Yuan, A. Fantetti, E. Denimal, S. Bhatnagar, L. Pesaresi, C. Schwingshackl, L. Salles, Propagation of friction parameter uncertainties in the nonlinear dynamic response of turbine blades with underplatform dampers, Mech. Syst. Signal Process. 156. doi:10.1016/j.ymssp.2021.107673. URL:https://doi.org/10.1016/j.ymssp.2021.107673..
[14] A. Ovcharenko, G. Halperin, I. Etsion, M. Varenberg, A novel test rig for in situ and real time optical measurement of the contact area evolution during pre-sliding of a spherical contact, Tribol. Lett. 23 (1) (2006) 55–63, https://doi.org/10.1007/s11249-006-9113-9.
[15] E. Diaconescu, M.L. Glovnea, Visualization and measurement of contact area by reflectivity, J. Tribol. 128 (4) (2006) 915–917, https://doi.org/10.1115/1.2345421.
[16] O. Ben-David, S.M. Rubinstein, J. Fineberg, Slip-stick and the evolution of frictional strength, Nature 463 (7277) (2010) 76–79, https://doi.org/10.1038/nature08676, URL:https://doi.org/10.1038/nature08676.
[17] B.A. Krick, J.R. Vail, B.N. Persson, W.G. Sawyer, Optical in situ micro tribometer for analysis of real contact area for contact mechanics, adhesion, and sliding experiments, Tribol. Lett. 45 (1) (2012) 185–194, https://doi.org/10.1007/s11249-011-9870-y.
[18] R. Sahli, G. Pallares, C. Ducottet, I.E. Ben Ali, S. Al Akhrass, M. Guibert, J. Scheibert, Evolution of real contact area under shear and the value of static friction of soft materials, Proc. Nat. Acad. Sci. USA 115 (3) (2018) 471–476, https://doi.org/10.1073/pnas.1706434115.
[19] J.H. Dieterich I, B.D. Kilgore, Direct Observation of Frictional Contacts: New Insights for State-dependent Properties, Tech. Rep. 3 (1994)..
[20] M. Lavella, D. Botto, M.M. Gola, Design of a high-precision, flat-on-flat fretting test apparatus with high temperature capability, Wear 302 (1–2) (2013) 1073–1081, https://doi.org/10.1016/j.wear.2013.01.066, URL:https://doi.org/10.1016/j.wear.2013.01.066.
[21] A. Fantetti, C. Pennisi, D. Botto, S. Zucca, C. Schwingshackl, Comparison of contact parameters measured with two different friction rigs for nonlinear dynamic analysis, in: International Conference on Noise and Vibration Engineering, 2020..
[22] T. Hoffmann, L. Panning, J. Wallaschek, Analysis of contacts in friction damped turbine blades using dimensionless numbers, J. Eng. Gas Turbines Power 141 (12). doi:10.1115/1.4044481. URL:https://asmedigitalcollection.asme.org/gasturbinespower/article/doi/10.1115/1.4044481/975419/Analysis-of-Contacts-in-Friction-Damped-Turbine..
[23] D. Botto, C. Gastaldi, M.M. Gola, M. Umer, An experimental investigation of the dynamics of a blade with two under-platform dampers, J. Eng. Gas Turbines Power 140 (3) (2017), https://doi.org/10.1115/1.4037865, URL:http://gasturbinespower.asmedigitalcollection.asme.org/article.aspx?doi=10.1115/1.4037865 032504.
[24] F. Hild, S. Roux, Digital image correlation: from displacement measurement to identification of elastic properties a review, Strain 42 (2006) 69–80.
[25] M.E. Kartal, D.M. Mulvihill, D. Nowell, D.A. Hills, Measurements of pressure and area dependent tangential contact stiffness between rough surfaces using digital image correlation, Tribol. Int. 44 (10) (2011) 1188–1198, https://doi.org/10.1016/j.triboint.2011.05.025, URL:https://doi.org/10.1016/j.triboint.2011.05.025.
[26] J. de Crevoisier, N. Swiergiel, L. Champaney, F. Hild, Identification of In Situ Frictional Properties of Bolted Assemblies with Digital Image Correlation, vol. 52, 2012. doi:10.1007/s11340-011-9518-8..
[27] L. Pesaresi, M. Stender, V. Ruffini, C. Schwingshackl, DIC measurement of the kinematics of a friction damper for turbine applications, in: Conference Proceedings of the Society for Experimental Mechanics Series, no. Dic, 2017..
[28] J. Juoksukangas, A. Lehtovaara, A. Mäntylä, Applying the digital image correlation method to fretting contact for slip measurement, in: Proceedings of the Institution of Mechanical Engineers, Part J: Journal of Engineering Tribology, vol. 231, SAGE Publications Ltd., 2017, pp. 509–519. doi:10.1177/1350650115601695..
[29] W. Chen, M. Jin, I. Lawal, M.R. Brake, H. Song, Measurement of slip and separation in jointed structures with non-flat interfaces, Mech. Syst. Signal Process. 134 (2019), https://doi.org/10.1016/j.ymssp.2019.106325, URL:https://linkinghub.elsevier.com/retrieve/pii/S0888327019305461 106325.
[30] M. Brøns, T.A. Kasper, G. Chauda, S.W. Klaassen, C.W. Schwingshackl, M.R. Brake, Experimental investigation of local dynamics in a bolted lap joint using digital image correlation, J. Vib. Acoust. (2020) 1–24, https://doi.org/10.1115/1.4047699, URL:https://asmedigitalcollection.asme.org/vibrationacoustics/article/doi/10.1115/1.4047699/1084970/Experimental-investigation-of-local-dynamics-in-a.
[31] C. Ferrer, F. Salas, M. Pascual, J. Orozco, Discrete acoustic emission waves during stick-slip friction between steel samples, Tribol. Int. 43 (1–2) (2010) 1–6, https://doi.org/10.1016/j.triboint.2009.02.009.
[32] Z. Geng, D. Puhan, T. Reddyhoff, Using acoustic emission to characterize friction and wear in dry sliding steel contacts, Tribiol. Int. 134 (2019) 394–407, https://doi.org/10.1016/j.triboint.2019.02.014, URL:https://doi.org/10.1016/j.triboint.2019.02.014.
[33] N.A. Emira, H.T. Mohamad, M.S. Tahat, Stick-slip detection through measurement of near field noise, Tech. Rep. 3 (2011), URL:http://www.academicjournals.org/jmer.
[34] C.L. Jiaa, D.A. Dornfeld, Experimental studies of sliding friction and wear via acoustic emission signal analysis, Wear 139 (2) (1990) 403–424, https://doi.org/10.1016/0043-1648(90)90059-J.
[35] R.S. Dwyer-Joyce, The application of ultrasonic NDT techniques in tribology (oct 2005). doi:10.1243/135065005X9763..

[36] G. Starzynski, R. Buczkowski, Ultrasonic measurements of contact stiffness between rough surfaces, J. Tribol. 136. doi:10.1115/1.4027132. URL:http://tribology.asmedigitalcollection.asme.org..
[37] J.Y. Kim, A. Baltazar, S.I. Rokhlin, Ultrasonic assessment of rough surface contact between solids from elastoplastic loading-unloading hysteresis cycle, J. Mech. Phys. Solids 52 (8) (2004) 1911–1934, https://doi.org/10.1016/j.jmps.2004.01.006.
[38] D.M. Mulvihill, H. Brunskill, M.E. Kartal, R.S. Dwyer-Joyce, D. Nowell, A comparison of contact stiffness measurements obtained by the digital image correlation and ultrasound techniques, Exp. Mech. 53 (7) (2013) 1245–1263, https://doi.org/10.1007/s11340-013-9718-5.
[39] B.W. Drinkwater, R.S. Dwyer-Joyce, P. Cawley, A study of the interaction between ultrasound and a partially contacting solid-solid interface, Proc. Roy. Soc. A Math. Phys. Eng. Sci. 452 (1996) 2613–2628. doi:10.1098/rspa.1996.0139..
[40] J. Baik, R.B. Thompson, Ultrasonic Scattering from Imperfect Interfaces: A Quasi-Static Model, Tech. rep. (1984).
[41] H. Xiao, Y. Sun, An improved virtual material based acoustic model for contact stiffness measurement of rough interface using ultrasound technique, Int. J. Solids Struct. doi:10.1016/j.ijsolstr.2018.07.026..
[42] M.B. Marshall, R. Lewis, R.S. Dwyer-Joyce, U. Olofsson, S. Björklund, Experimental characterization of wheel-rail contact patch evolution, J. Tribol. 128 (3) (2006) 493–504, https://doi.org/10.1115/1.2197523.
[43] J. Krolikowski, J. Szczepek, Prediction method of contact parameters using ultrasonic method, Wear 148 (1991) 181–195.
[44] A. Baltazar, S.I. Rokhlin, C. Pecorari, On the relationship between ultrasonic and micromechanical properties of contacting rough surfaces, J. Mech. Phys. Solids 50 (7) (2002) 1397–1416, https://doi.org/10.1016/S0022-5096(01)00119-3.
[45] K. Kendall, D. Tabor, An ultrasonic study of the area of contact between stationary and sliding surfaces, Proc. Roy. Soc. A Math., Phys. Eng. Sci. 323 (1971) 321–340. doi:10.1098/rspa.1971.0108..
[46] L. Pesaresi, A. Fantetti, F. Cegla, L. Salles, C. Schwingshackl, On the use of ultrasound waves to monitor the local dynamics of friction joints, Exp. Mech. 60 (1) (2020) 129–141, https://doi.org/10.1007/s11340-019-00550-y, URL:http://link.springer.com/10.1007/s11340-019-00550-y.
[47] A. Takeuchi, Detection of operational abnormality of ball bearing with ultrasonic technique, Key Eng. Mater. 270–273 (2009) 252–257, https://doi.org/10.4028/www.scientific.net/kem.270-273.252.
[48] H.G. Tattersall, The ultrasonic pulse-echo technique as applied to adhesion testing, J. Phys. D: Appl. Phys. 6 (7) (1973) 819–832, https://doi.org/10.1088/0022-3727/6/7/305.
[49] H.-S. Ahn, D.-I. Kim, In situ evaluation of wear surface by ultrasound, Tech. rep. (2001)..
[50] H. Brunskill, A. Hunter, L. Zhou, R. Dwyer Joyce, R. Lewis, An evaluation of ultrasonic arrays for the static and dynamic measurement of wheelrail contact pressure and area, Proc. Inst. Mech. Eng. J: J. Eng. Tribol. doi:10.1177/1350650120919889..
[51] R.S. Dwyer-Joyce, B.W. Drinkwater, A.M. Quinn, The use of ultrasound in the investigation of rough surface interfaces, J. Tribol. 123 (1) (2001) 8, https://doi.org/10.1115/1.1330740, URL:http://tribology.asmedigitalcollection.asme.org/article.aspx?articleid=1466266.
[52] A. Fantetti, C. Schwingshackl, Effect of friction on the structural dynamics of built-up structures: an experimental study, in: Proceedings of the ASME Turbo Expo 2020: Turbomachinery Technical Conference and Exposition. Volume 11: Structures and Dynamics: Structural Mechanics, Vibration, and Damping; Supercritical CO2, 2020..
[53] C. Gastaldi, T. Berruti, M.M. Gola, The effect of surface finish on the proper functioning of underplatform dampers, J. Vib. Acoust. (2020) 1–30, https://doi.org/10.1115/1.4046954.
[54] P. Berthoud, T. Baumberger, Shear stiffness of a solid-solid multicontact interface, in: Procedures Royal Society London, no. 454, 1998, pp. 1615–1634. doi:10.1098/rspa.1998.0223..
[55] D.J. Dickrell III, W.G. Sawyer, Lateral contact stiffness and the elastic foundation, Tribol. Lett. 41 (2011) 17–21, https://doi.org/10.1007/s11249-010-9666-5.
[56] T. Fujimoto, J. Kagami, T. Kawaguchi, T. Hatazawa, Micro-displacement characteristics under tangential force, Wear 241 (2) (2000) 136–142, https://doi.org/10.1016/S0043-1648(00)00385-9.
[57] S.M. Lee, M.W. Shin, W.K. Lee, H. Jang, The correlation between contact stiffness and stick-slip of brake friction materials, Wear 302 (2013) 1414–1420, https://doi.org/10.1016/j.wear.2012.12.017, URL:https://doi.org/10.1016/j.wear.2012.12.017.
[58] A. Papangelo, N. Hoffmann, M. Ciavarella, Load-separation curves for the contact of self-affine rough surfaces, Sci. Rep. 7 (1) (2017) 4–10, https://doi.org/10.1038/s41598-017-07234-4.
[59] M. Gonzalez-Valadez, A. Baltazar, R. Dwyer-Joyce, Study of interfacial stiffness ratio of a rough surface in contact using a spring model, Wear 268 (3–4) (2010) 373–379, https://doi.org/10.1016/j.wear.2009.08.022, URL:http://www.sciencedirect.com/science/article/pii/S0043164809005092.
[60] R. Thomas, B.W. Drinkwater, D. Liaptsis, The reflection of ultrasound from partially contacting rough surfaces, J. Acoust. Soc. Am. 117 (2) (2005) 638–645, https://doi.org/10.1121/1.1835505.
[61] F.P. Bowden, D. Tabor, The Friction and Lubrication of Solids, vol. 1, Clarendon, Oxford, 1950.
[62] S.M. Rubinstein, G. Cohen, J. Fineberg, Contact area measurements reveal loading-history dependence of static friction, Phys. Rev. Lett. 96 (25). doi:10.1103/PhysRevLett.96.256103..
[63] L. Pei, S. Hyun, J.F. Molinari, M.O. Robbins, Finite element modeling of elasto-plastic contact between rough surfaces, J. Mech. Phys. Solids 53 (11) (2005) 2385–2409, https://doi.org/10.1016/j.jmps.2005.06.008.
[64] J. Wang, T. Chen, X.P. Wang, Y. Xi, Dynamic identification of tangential contact stiffness by using friction damping in moving contact, Tribol. Int. doi:10.1016/j.triboint.2018.10.028..
[65] K.-H. Koh, J.H. Griffin, S. Filippi, A. Akay, Characterization of turbine blade friction dampers, J. Eng. Gas Turbines Power 127 (4) (2005) 856, https://doi.org/10.1115/1.1926312, URL:http://gasturbinespower.asmedigitalcollection.asme.org/article.aspx?articleid=1423184.
[66] J. Wu, R. Yuan, Z. He, D. Zhang, Y. Xie, Experimental study on dry friction damping characteristics of the steam turbine blade material with nonconforming contacts, Adv. Mater. Sci. Eng. doi:10.1155/2015/849253..
[67] D. Tabor, Junction growth in metallic friction: the role of combined stresses and surface contamination, Procedures Roy. Soc. Lond., Ser. A 251 (1959) 378–393.
[68] E. Rabinowicz, The nature of the static and kinetic coefficients of friction, J. Appl. Phys. 22 (11) (1951) 1373–1379, https://doi.org/10.1063/1.1699869.
[69] J.S. Courtney-Pratt, E. Eisner, The effect of a tangential force on the contact of metallic bodies, Proc. Roy. Soc. A: Math., Phys. Eng. Sci. 238 (1215) (1957) 529–550, https://doi.org/10.1098/rspa.1957.0016.
[70] T. Baumberger, C. Caroli, Solid friction from stick-slip down to pinning and aging, Adv. Phys. 55 (3–4) (2006) 279–348, https://doi.org/10.1080/00018730600732186, arXiv:0506657.
[71] Q. Li, T.E. Tullis, D. Goldsby, R.W. Carpick, Frictional ageing from interfacial bonding and the origins of rate and state friction, Nature 480 (7376) (2011) 233–236, https://doi.org/10.1038/nature10589.
[72] Y. Bar-Sinai, M. Aldam, R. Spatschek, E.A. Brener, E. Bouchbinder, Spatiotemporal dynamics of frictional systems: the interplay of interfacial friction and bulk elasticity, Lubricants 7 (10). doi:10.3390/lubricants7100091..
[73] J. Wojewoda, R. Barron, Chaotic behaviour of friction force, Int. J. Bifurcation Chaos 2 (1)..
[74] P. Huthwaite, Accelerated finite element elastodynamic simulations using the GPU, J. Comput. Phys. 257 (2014) 687–707.
[75] F. Moser, L. Jacobs, J. Qu, Modeling elastic wave propagation in waveguides with the finite element method, NDT & E Int. 32 (4) (1999) 225–234.
[76] R. Courant, K. Friedrichs, H. Lewy, On the partial difference equations of mathematical physics, IBM J. 11 (2) (1967) 215–234.
[77] A. Raghavan, C.E. Cesnik, Finite-dimensional piezoelectric transducer modeling for guided wave based structural health monitoring, Smart Mater. Struct. 14 (6)..